Department of Physics and Astronomy

Heidelberg University

Bachelor thesis

in Physics

submitted by

Stephan Lachnit

born in Heidelberg (Germany)

2021

Pulse Shape Characterization and Allpix Squared Simulation of the MuPix10

This Bachelor thesis has been carried out by

Stephan Lachnit

at the

Physikalisches Institut

under the supervision of

Prof. André Schöning

Abstract

The Mu3e experiment will search for the charged lepton flavor violating $\mu \to eee$ decay, which requires a detector with a high momentum, vertex and time resolution. To reduce the impact of multiple Coulomb scattering strict limits are imposed on the available material budget. High-Voltage Monolithic Active Pixel Sensors were chosen to fulfill these requirements, with the MuPix10 being the first sensor to meet all design requirements. To efficiently detect a traversing particle, it implements a Charge Sensitive Amplifier in combination with a Time-over-Threshold logic to digitize hit information.
Monte Carlo simulations can be used to gain a deeper understanding of detector response and can be used to verify data and improve future detectors. The Allpix^2 simulation framework is specifically targeted at pixel sensors such as the MuPix10.
In this thesis, the pulse shape of the MuPix10 is characterized from measurements and a simplified model for the shape is developed. A calibration is done using ^{55}Fe. The pulse shape model is implemented in Allpix^2 and a comparison between measurements with ^{90}Sr and the simulation is made. Overall the simulation matches with the measured data.

Zusammenfassung

Das Mu3e Experiment plant nach dem geladenen Leptonfamilienzahl verletzenden $\mu \to eee$ Zerfall zu suchen, was einen Detektor mit hoher Impuls-, Vertex- und Zeitauflösung benötigt. Um die Auswirkungen von Mehrfachstreuung zu reduzieren, ist das verfügbare Materialbudget stark begrenzt. Hochspannungsbetriebene monolithische aktive Pixelsensoren wurden ausgewählt um diese Anforderung zu erfüllen, wobei der MuPix10 der erste Sensor ist, der alle Designanforderungen erfüllt. Um durchquerende Teilchen mit hoher Effizienz zu detektieren, sind ein ladungsempfindlicher Verstärker und eine Zeit-über-Schwellwert-Logik zur Digitalisierung der Trefferinformationen verbaut.
Monte-Carlo-Simulationen können herangezogen werden um ein tieferes Verständnis der Detektorantwort zu erlangen, um Daten zu verifizieren und um zukünftige Detektoren zu verbessern. Das Simulationsframework Allpix^2 ist speziell auf Pixelsensoren wie den MuPix10 ausgerichtet.
In dieser Arbeit wird die Pulsform des MuPix10 durch Messungen charakterisiert und vereinfacht modelliert. Eine Kalibrierung mit ^{55}Fe wird durchgeführt. Das Pulsformmodell wird in Allpix^2 implementiert und die Messungen mit ^{90}Sr mit der Simulation verglichen. Die Simulation stimmt weitgehend mit den gemessenen Daten überein.

Contents

Chapter 1

Introduction

1.1 Motivation

The Standard Model of particle physics is one of the most precise theories ever formulated in the field of physics. Its properties are continuously measured and several of its predictions have been verified. Despite the experimental success of the theory, it still has unanswered questions. For example, it does not include gravity as a fundamental force and requires numerous seemingly arbitrary constants. To solve these pending issues, new theories can be verified by searching for deviations between experiments and predictions.

One of such experiments is Mu3e [1], which searches for the charged lepton flavor violating $\mu \rightarrow eee$ decay, which would be a strong indicator for physics beyond the Standard Model. To achieve a high sensitivity for this decay, high precision measurements of the decay particles are required. Due to the relatively low energy of the electrons from the muon decay, the experiment places strict constraints on the material budget of the tracking system. For this reason High-Voltage Monolithic Active Pixel Sensors (HV-MAPS) are used as vertex detectors. The MuPix sensors are specifically being developed for this experiment, with the MuPix10 being the first sensor to fulfill all design requirements.

Being able to simulate the outcome of an experiment and compare it to measurements can help to understand and verify the experimental results. Monte Carlo simulations for particle physics have long been developed and used. There are precise simulation toolkits, like Geant4, that can accurately simulate how particles behave in matter. However, these precise simulation lack the digital readout implementation of HV-MAPS, making them unprofitable as a standalone simulation. Allpix^2 is a simulation framework that was specifically made for this purpose, combining Geant4 with efficient readout simulation.

Writing simulations requires a good understanding of the detector readout chain, and in case of the MuPix10 the pulse shaping of the amplifier. To build a model for the pulse shape, the pulse shape is measured for fixed signals induced by artificial charge injection. To convert between the injection and real charge, a calibration needs to be done, for which ^{55}Fe was chosen. Finally, the calibrated pulse shape model can be used to compare measurements with simulations. In this thesis, the model is implemented in Allpix^2 and the results of the simulation are compared with a ^{90}Sr source.

1.2 The Standard Model

The Standard Model (SM) of particle physics is a theory that describes particles and their interactions, summarized in Figure 1.1. Forces are carried by gauge bosons (spin 1), and include the electromagnetic force (carried by the photon), the weak force (carried by the Z and W bosons), and the strong force (carried by gluons). Matter is covered by fermions (spin $\frac{1}{2}$), which exist in three generations and can be divided into quarks and leptons. Unlike leptons, quarks have a color charge and interact with the strong force. Each fermion also has a matching antiparticle, which has the same mass and spin, but opposite generalized charge. There is also the Higgs boson (spin 0), which gives the particles its mass via the Higgs mechanism.

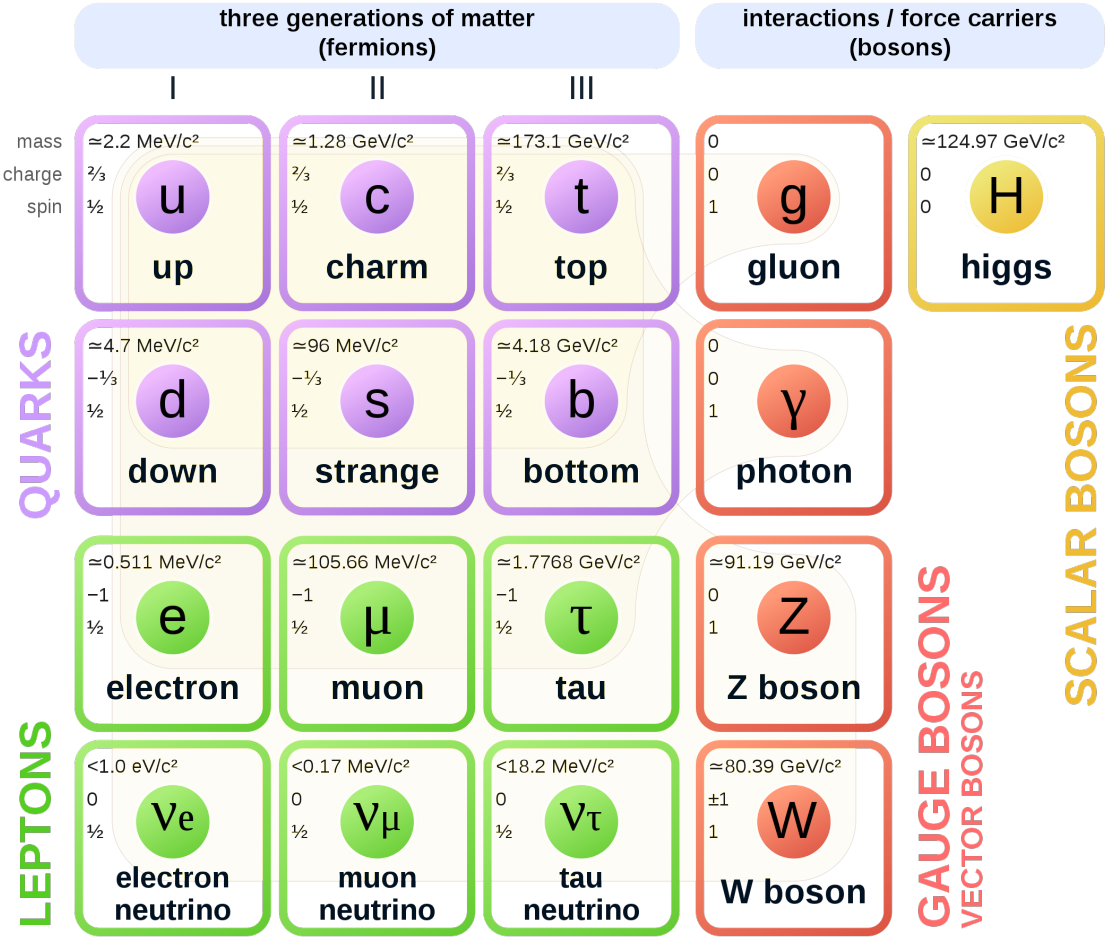

Figure 1.1: Particles in the Standard Model. Taken from [2].

Interactions in the Standard Model can be represented by Feynman diagrams (e.g. Figure 1.3). The Standard Model has several conservation laws for these interactions, such as charge, lepton flavor and baryon numbers. These conserved quantities must be conserved in all particle interactions, which correspond to vertices in Feynman diagrams.
However, several experiments observed oscillations between different neutrino flavors (e.g. [3]). These observations of lepton flavor violations (LFVs) generate interest in searching for LFVs in other leptons, such as the muon.

1.3 Muon Decay

In the Standard Model, the dominant decay for muons and antimuons is the Michel decay $\mu^- \to \nu_\mu e^- \bar{\nu}_e$ and $\mu^+ \to \bar{\nu}_\mu e^+ \nu_e$ (Figure 1.2), which has a branching ratio close to 100 % [4]. With neutrino oscillations, the decay $\mu^+ \to e^+ e^- e^+$ is possible (Figure 1.3a), but the theoretical branching ratio of this decay is very small ($\ll 10^{-50}$) [5]. Because of this small branching ratio, any observation of the $\mu \to eee$ decay would constitute a crucial proof of LFV [1].
Looking at the SM, an experiment designed to investigate the $\mu \to eee$ decay channel may have other sources of background to consider. In particular, given the difficulty to experimentally reconstruct neutrinos, internal conversion ($\mu^+ \to e^+ e^- e^+ \bar{\nu}_\mu \nu_e$) might produce background. Here, the positron from the Michel decay emits a virtual photon which decays into an electron-positron pair.

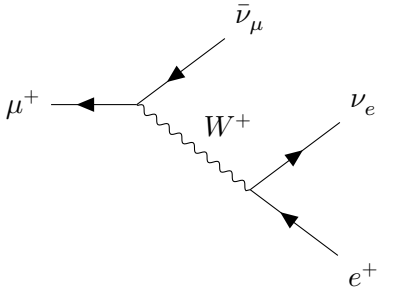

Figure 1.2: Michel decay.

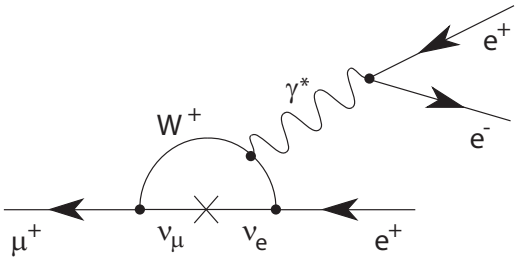

(a) SM $\mu^+ \to e^+ e^- e^+$ decay via Neutrino Oscillation. Taken from [1].

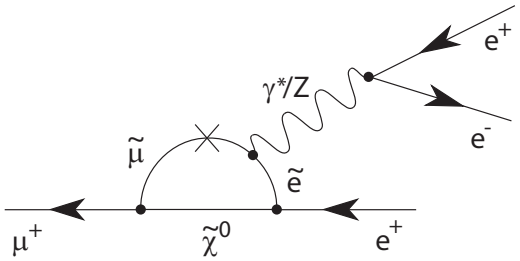

(b) SUSY $\mu^+ \to e^+ e^- e^+$ decay via supersymmetric particles. Taken from [1].

Figure 1.3: Feynman diagrams for $\mu \to eee$ decays.

While LFVs have been observed for neutrinos, they haven't yet been observed for charged leptons. Some Beyond Standard Model (BSM) theories predict higher branching ratios than the Standard Model for charged lepton flavor violations (CLFVs). One of these BSM theories is Supersymmetry (SUSY). SUSY introduces new particles which would allow CLFV decays. An example of such a CLFV with muons is shown in Figure 1.3b. Due to the low SM background, measuring a CLFV would be a strong indicator for BSM physics like SUSY.

1.4 Mu3e Experiment

The Mu3e experiment is a particle physics experiment at the Paul Scherrer Institute (PSI) in Villigen, Switzerland. The main purpose of Mu3e is to search for the CLFV decay $\mu^+ \to e^+ e^- e^+$ using a muon beam stopped onto a fixed target. The branching ratio sensitivity is aimed to be 2×10^{-15} in its first phase [7], and it is planned to be increased to 1×10^{-16} in the Phase II of the experiment [1]. To achieve this sensitivity, a high intensity muon beam is required. The muon beam line at PSI has a particle rate of about 100 MHz, which is sufficient for Phase I. For Phase II a new high intensity muon beamline is planned with a particle rate of 2 GHz.

Figure 1.4: Mu3e Logo [6].

The current upper limit for the branching ratio of the $\mu^+ \to e^+ e^- e^+$ decay is 1×10^{-12}, which was set by the SINDRUM experiment in 1988 [8]. The search for CLFV decays has a long history of experiments, and several other experiments are planned to search for CLFV decays with higher precision (see Figure 1.5).

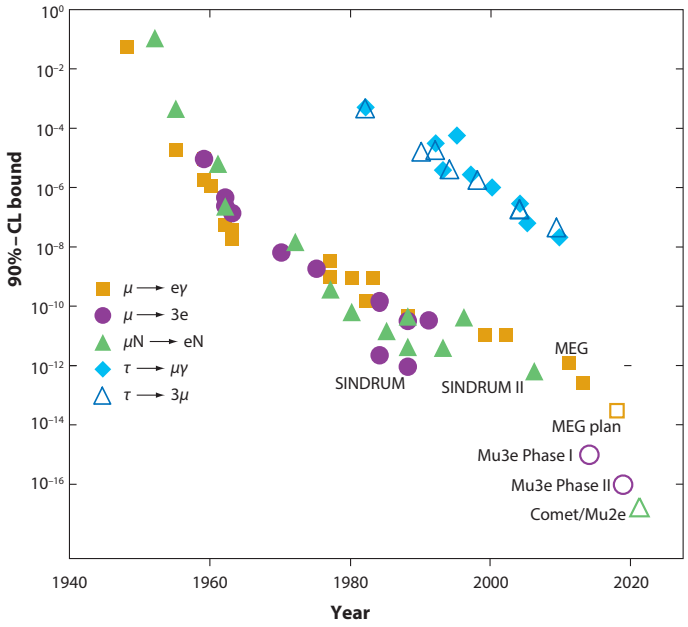

Figure 1.5: Past and future LFV experiments [6]. Modified from [9].

1.4.1 Signal and Background

For a muon in the rest frame, the total momentum of the system is zero and the total energy of the system is equal to the rest energy of the muon, $E_0 = m_\mu c^2 \simeq 106\,\text{MeV}$.
Due to momentum and energy conservation, no decay product of a $\mu \to eee$ decay can exceed half the rest energy of the muon, i.e. 53 MeV. In addition to that, all decay products have to originate from the same point in space-time.
These constraints can be used to suppress background events, which are of two types: accidental and irreducible.

Accidental Background

Accidental backgrounds events happen when two different Michel decays are combined like a $\mu \to eee$ decay. This can happen due to the high muon rates and limited detector resolution. Examples are given in Figure 1.6. In Figure 1.6a a Michel decay is combined with a decay through internal conversion, where one positron has too little momentum to be detected, creating a fake signal. Similarly in Figure 1.6b the positrons from two Michel decays combined with an electron from Bhabha scattering create a fake signal. Bhabha scattering can occur when positrons from the decay interact with the electrons in the detector material.

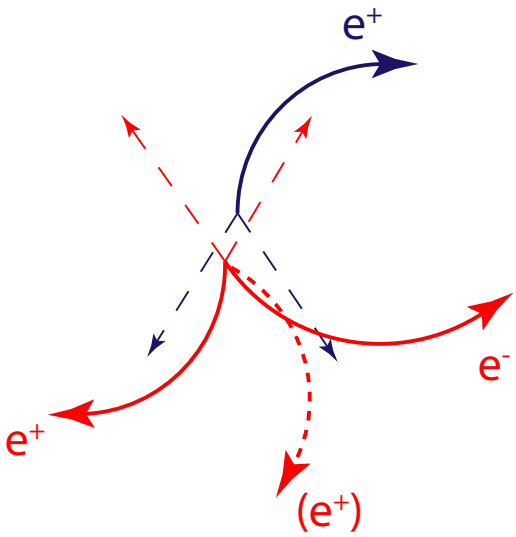

(a) Michel decay (blue) combined with an internal conversion decay (red) [6].

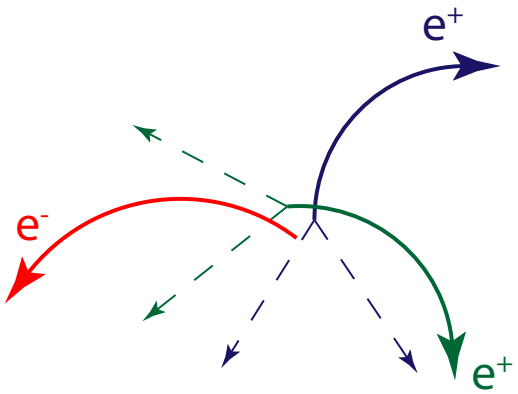

(b) Two Michel decays (blue, green) combined with Bhabha scattering (red) [6].

Figure 1.6: Accidental combinatorial backgrounds.

Irreducible Background

The irreducible background in the Mu3e experiment consists of the internal conversion decay $\mu^+ \to e^+ e^- e^+ \bar{\nu}_\mu \nu_e$. As detecting neutrinos with a high efficiency is infeasible and are not thus detected in the Mu3e detector, the decay can only be discriminated from a real $\mu^+ \to e^+ e^- e^+$ decay through the missing momentum of the neutrinos. To detect the missing momentum, the detector needs a momentum resolution of at least 1 MeV/c [7].

1.4.2 Detector

The Mu3e detector is a cylinder where the muon beam is its symmetry axis with the target in the center. It is designed to have a high momentum, position and time resolution to distinguish the signal from the background, while also using as little material as possible to reduce multiple scattering (see subsection 1.5.3).
The entire detector is placed in a 1 T magnetic field. This bends the tracks of the decay products, which due to their low energy have a small bend radius and get curled back into the detector. This allows particles to be measured again, such that one can calculate the bend radius and increase the momentum resolution of the detector. It also allows to distinguish between electrons and positrons, which due to their opposite charge bend in

opposite directions in the magnetic field.
The two innermost layers around the target consists of pixel detectors, which are surrounded by scintillating fibers and an outer pixel layer. The scintillating fiber detector (SciFi) has a time resolution of about 250 ps.
Upstream and downstream of the target are additional "recurl stations" with pixels and a scintillating tile detector. The scintillating tiles are read out by Silicon Photon Multipliers (SiPM). The tile detector has a time resolution of about 50 ps.
Due to the low energy of the decay products, multiple coulomb scattering is a concern. It is therefore important to design a detector with a small material budget. The estimated material budget is 0.1 % X_0 for a pixel layer and 0.2 % X_0 for the SciFi. The detector is cooled with gaseous helium, which provides adequate cooling with little multiple Coulomb scattering. Since the tile detector is at the end of the trajectory of the recurling particles, material budget is not important for this component.

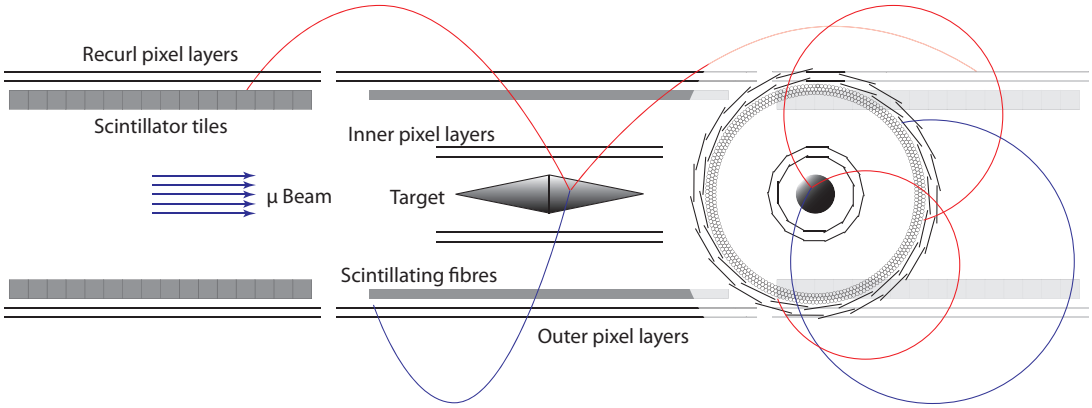

Figure 1.7: Schematic view of the Mu3e detector with a $\mu \to eee$ event [6].

1.5 Particle Interaction with Matter

Particles can only be measured when they interact with the detector. Since interactions can also change the energy and trajectory of the particle, understanding how particles behave in matter is a key factor in designing detectors for particle physics experiments. Since the goal of the Mu3e experiment is measuring leptons, which interact via the electromagnetic force with matter, only the electromagnetic force will be discussed in this section. Hadrons and their interactions with the strong force are not discussed.
When leptons travel through matter, they can lose kinetic energy in various ways, mainly through scattering, ionization and Bremsstrahlung. This energy loss depends on various factors, such as the charge and energy of the particle or the material they traverse.

1.5.1 Heavy Charged Particles

Particles with a mass larger than electrons are usually called "heavy particles". When these particles travel through matter, their most significant energy loss is from ionization of the material. The mean energy loss per traveled distance can be described with the Bethe-Bloch formula [10, 11] given in Equation 1.1.

$$-\left\langle \frac{\mathrm{d}E}{\mathrm{d}x} \right\rangle = \frac{4\pi n z^2}{m_\mathrm{e} c^2 \beta^2} \cdot \left(\frac{e^2}{4\pi\varepsilon_0} \right)^2 \cdot \left[\log\left(\frac{2 m_\mathrm{e} c^2 \beta^2}{I \cdot (1-\beta^2)} \right) - \beta^2 - \frac{\delta(\beta\gamma)}{2} \right] \tag{1.1}$$

With the following parameters and constants:

- n: electron density in the material
- z: charge of traversing particle in multiples of e
- m_e: rest mass of the electron
- c: speed of light in vacuum
- β: relative velocity $\beta = \frac{v}{c}$ of the traversing particle
- v: velocity of the traversing particle
- e: elementary charge
- ε_0: vacuum permittivity
- I: mean excitation energy of the material
- $\delta(\beta\gamma)$: density effect correction
- γ: Lorentz factor $\gamma = \frac{1}{\sqrt{1-\beta^2}}$ of the traversing particle

In Figure 1.8 the mean energy loss as described by the Bethe-Bloch formula is shown for different materials. The curves have a minimum at around $\beta\gamma \simeq 3$. This means for every particle there is certain energy where it looses the least amount of energy when traversing the material. This is called the minimum ionizing energy of the particle and the particle traversing the material with this energy a Minimum Ionizing Particle (MIP).
For lower momenta the energy loss increases because the interaction time with the material increases. This causes an energy loss that is roughly proportional to β^{-2}. For higher momenta relativistic effects become more significant, resulting in a logarithmic rise of the energy loss. The electric field gets compressed along the longitudinal axis, which leads to a higher interaction strength perpendicular to the direction of the particles momentum.

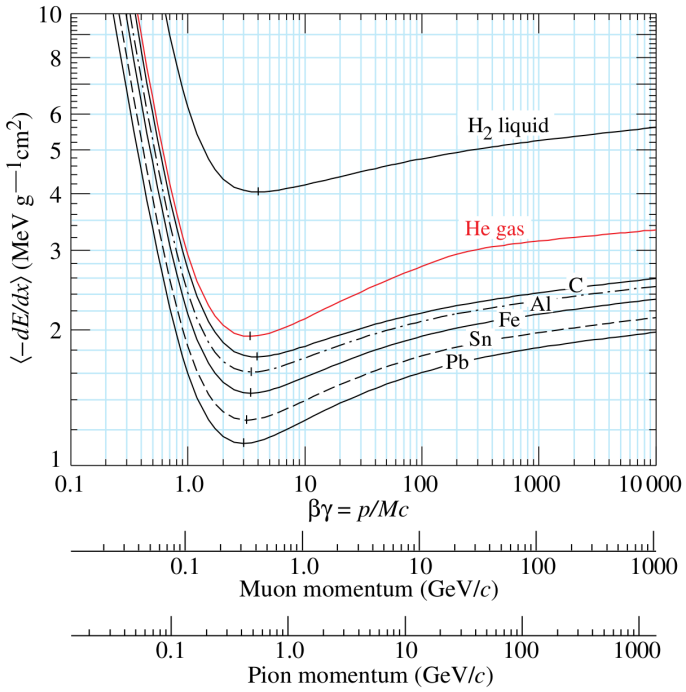

Figure 1.8: Mean energy loss of heavy particles for different materials. Taken from [11].

1.5.2 Electrons and Positrons

For electrons and positrons there are two more effects in addition to ionization that contribute to energy loss. The effect of Bremsstrahlung has a higher influence on lighter particles and is not described by the Bethe-Bloch formula.
In addition electrons experience electron degeneracy pressure from the electrons in the material (also called Fermi pressure). This is a result of the Pauli exclusion principle, which states that two identical fermions cannot occupy the same quantum sate.
In contrast to electrons, positrons can annihilate with the electrons in the material. This leads to a difference in the mean energy loss for electrons and positrons. The Berger-Seltzer formula [12] given in Equation 1.2 accounts for these effects.

$$-\left\langle \frac{\mathrm{d}E}{\mathrm{d}x} \right\rangle = \rho \frac{0.153536}{\beta^2} \frac{Z}{A} \left(B_0(T) - 2\log\left(\frac{I}{m_e c^2} \right) - \delta \right) \tag{1.2}$$

With the following parameters and constants in addition to what is listed for Equation 1.1:

- ρ: density of the material
- $\frac{Z}{A}$: ratio of protons to nucleons in the material
- $B_0(T)$: particle momentum dependent stopping power of the material
- δ: density correction for electrons or positrons

In Figure 1.9 the energy loss of electrons and positrons in silicon is plotted as function of their momentum. The curves for the two particles follow a similar behavior, but there is a small difference, especially for higher momenta. The energy loss for electrons is higher due to the repulsion from the electrons in the material as described above.

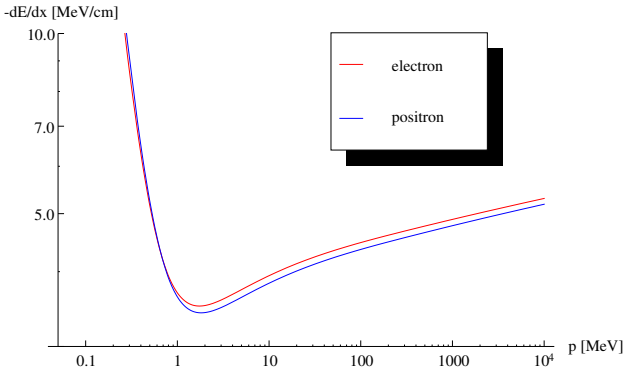

Figure 1.9: Mean energy loss for electrons and positrons in silicon. Taken from [13].

1.5.3 Multiple Coulomb Scattering

In addition to energy loss effects, particles traversing matter can also undergo deflection of their trajectory. Coulomb scattering occurs when a charged particle scatters off a Coulomb field from a nucleus. This scattering process can happen multiple times in a material and can be described as a net angle deflection (Figure 1.10). The root mean square of the angular deflection approximated by a Gaussian distribution can be described using the Highland equation [14, 11] given in Equation 1.3.

$$\Theta_{\text{rms}} = \frac{13.6\,\text{MeV}}{\beta cp} z \sqrt{\frac{x}{X_0}} \left(1 + 0.038 \log\left(\frac{x}{X_0}\right)\right) \tag{1.3}$$

With the following parameters and constants in addition to what is listed for Equation 1.1:

- x: distance traveled in the material
- X_0: radiation length of the material

Multiple Coulomb scattering in a detector changes the trajectory of a particle and thus limits the achievable resolution. Since the small momenta of the leptons in the Mu3e experiment increase the scattering angle, multiple Coulomb scattering is a major concern. To reduce it, the traveled distance x needs to be as small as possible, which imposes constraints on the thickness of the detector.

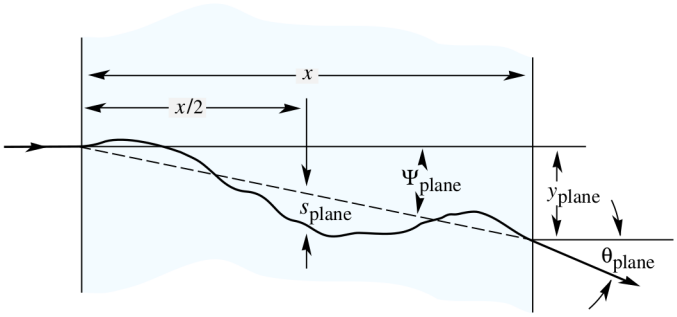

Figure 1.10: Multiple Coulomb Scattering. Taken from [11].

1.5.4 Photons

Photons can interact with matter in various processes, which depend on the energy of the photons and the atomic properties and density of the material they traverse. In Figure 1.11 the cross section of different processes in silicon in given as a function of the photon energy.

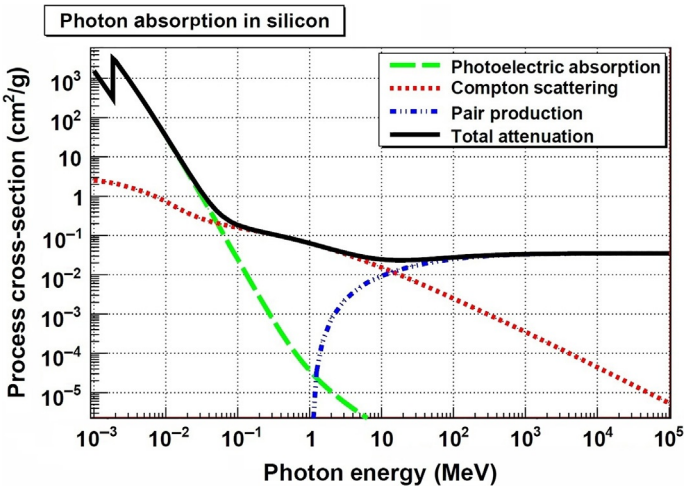

Figure 1.11: Photon absorption in silicon. Taken from [15].

In the energy regions relevant for the MuPix10 (about 10 keV), the photoelectric effect is the most dominant interaction. Here, a photon triggers the emission of an electron from an atom and is absorbed in the process. The photon energy required for this process depends on the material.
At higher energies, photons experiencing Compton scattering scatter of an electron and loses energy in the process, but are not absorbed. The shift in wavelength depends on the angle by which the photon is scattered at.
Finally, when the energy of a photon is higher than twice the electron mass (about 1 MeV), the photon can be converted into an electron-positron pair through the pair production process. To satisfy conservation of momentum, a nucleus must be nearby.

1.6 Semiconductor Physics

The movement of electrons in materials can be modeled with so-called energy bands. The valence band is the highest occupied band at a temperature of $T = 0\,\mathrm{K}$, where all electrons are in the lowest possible energy state. The conduction band is the energy band above the valence band, where electric conduction can happen.
There are three categories of materials with respect to these energy bands: insulators, conductors and semiconductors. Insulators have a large energy gap between the valence band and the conduction band. For conductors, on the other hand, the valence and conduction band overlap are identical.
Semiconductors have a band gap between the valence and conduction band, which is small enough so that electrons can move to the conduction band through thermal excitation. Their conductivity thus increases with temperature. If an electron gets excited to the conduction band it leaves behind a so-called "hole", which can be filled from another electron in the valence band or recombined with an electron from the conduction band. This means that in a semiconductors both electrons and holes are charge carriers.

1.6.1 Silicon

Silicon is the most common material for semiconductors and also used for the Mupix10 sensor. It has four valence electrons and forms a diamond-like lattice. Its band gap is small enough that electrons can jump between band gaps at room temperature. However, the charge carrier density of intrinsic silicon is so low compared to the atomic density, that it acts like an insulator. A process called doping can be used to increase the charge carrier density. The average energy required to create an electron-hole pair is about 3.64 eV [16].

1.6.2 Doping

Doping is the process of purposely adding impurities to a semiconductor lattice to increase its charge carrier density. Doped semiconductors are also called extrinsic semiconductors. When adding phosphorus, which has five valence electrons, to a silicon lattice, the additional electron is released to the conduction band. Materials that add negative charge carriers such as phosphorus are called donors, and the semiconductor n-doped.
Similarly, boron with its three valence electrons can be used to add a hole into the silicon lattice. Neighboring valence electrons can then fill the hole, resulting in a hole as free charge carrier. Materials that create positive charge carriers like boron are called acceptors, and the semiconductor p-doped.

1.6.3 p-n Junction

When a p-doped region in a semiconductor is side-by-side to an n-doped region, the contact region is called a p-n junction. At the border electrons from the n-doped region diffuse into the p-doped region and holes from the p-doped region diffuse into the n-doped region. This creates a diffusion current, which induces a net positive charge in the n-doped region and a net negative charge in the p-doped region.
The induced charge difference then generates an electric field, which creates a drift current in the opposite direction of the diffusion current until equilibrium is reached. Free charges in the electric field either drift away or recombine with other charges.
As a result a region with barely any free charges emerges, which is called depletion zone. Its width can be increased or decreased by applying a so-called bias voltage. If the p-doped region is connected to a positive terminal and the n-doped region to a negative terminal, it

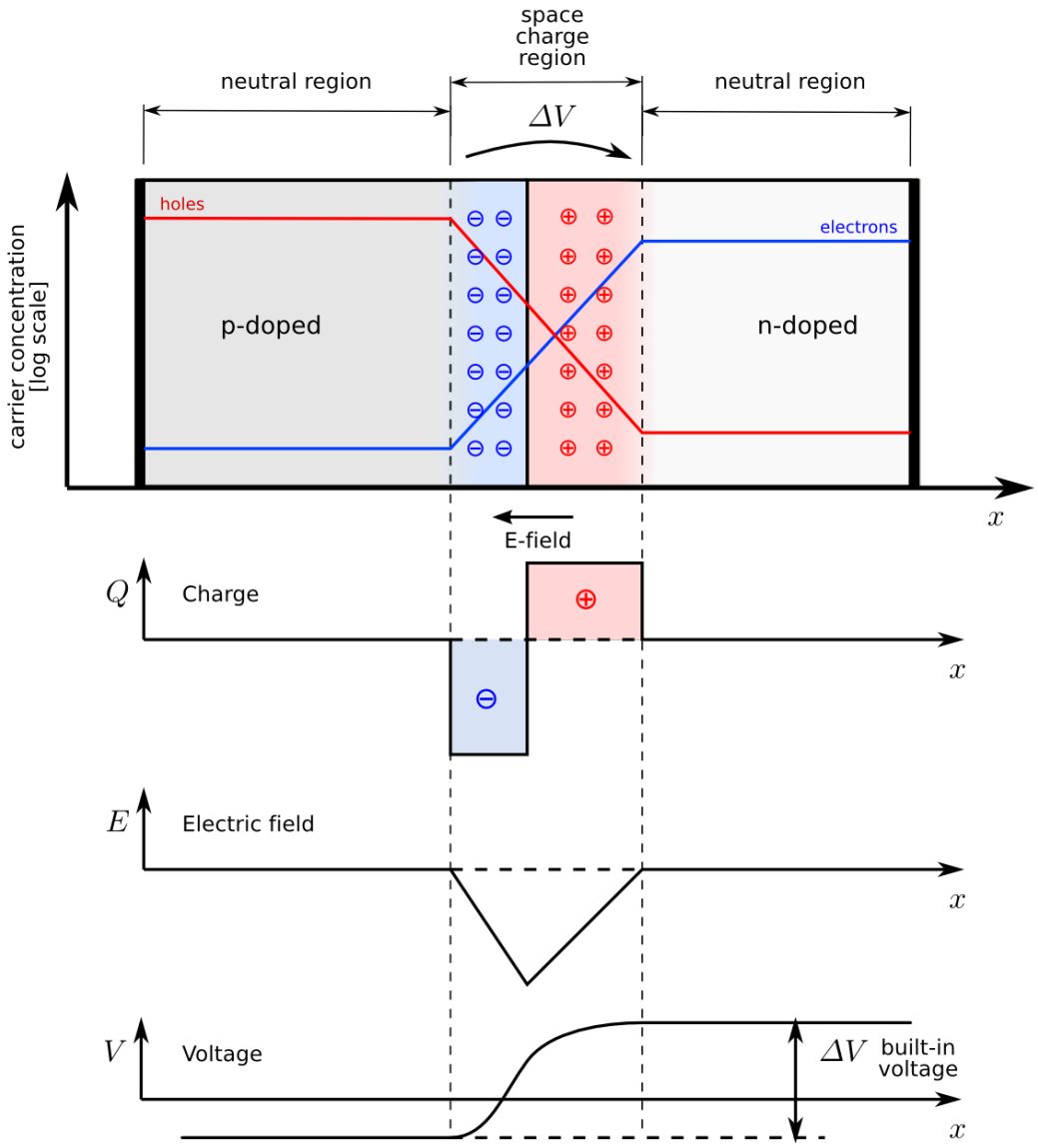

Figure 1.12: Overview of a p-n junction in equilibrium. Taken from [17].

is called a forward bias. Due to the potential difference, the diffusion force towards the depletion zone increases and the width of the depletion zone decreases. For a reverse bias, the n-doped region is connected to the positive terminal and the p-doped region to the negative. The applied voltage decreases the diffusion force and the width of the depletion zone increases.

1.7 Semiconductor Detectors

Semiconductor particle detectors use the properties of a p-n junction described in subsection 1.6.3 to detect particles. With the processes described in section 1.5, traversing particles can create electron-hole pairs in the semiconductor. If the creation of the electron-hole pair happens outside of the depletion zone, most charges will simply recombine. However if it happens within the depletion zone, the charges generate a detectable current. Due to the electric field in the depletion zone, electrons and holes drift in opposite directions. The electrons travel to the anode of the sensor, where they create a small current. This current can be picked up by a capacity and amplified through a charge sensitive amplifier. Since detectors based on semiconductors can be made very small, they are often used as vertex detectors close to the interaction point.

1.7.1 Pixel Sensors

One type of semiconductor detectors are pixel detectors. Each pixel has its own separated p-n junction. If a charged particle traverses the detector, its position can be determined from the pixels that fired. If the magnitude of the signal in the fired pixels is known, the energy released by the particle can be estimated.

Hybrid Sensors Hybrid pixel sensors consist of two entities. One is the sensor diode with the pixels. Here a high voltage is applied as reverse bias to increase the width of the depletion zone as much as possible. The other one has the readout electronics. One advantage of hybrid pixels sensor is that the sensor diode and the readout chip are separated and only bond together with solder bumps. This shields the readout circuits from the high electric field in the sensor diode. It also allows to use different materials for the sensor diode like germanium while using a silicon chip for the readout.

Active Pixel Sensors Active Pixel Sensors (APS) have so-called active pixels. This means that the amplification of the collected charges happens inside the pixel. This has the advantage that the charges are not moved to the readout electronics, which results in a reduced noise level. APS still require dedicated readout electronics.

Monolithic Active Pixel Sensors Monolithic Active Pixel Sensors (MAPS) are an advancement of APS developed for applications where material budget is a tight constraint. Compared to APS, MAPS also include a full readout implementation in the chip. Since this means a separate readout chip can be omitted, MAPS can be made thinner than hybrid pixel sensors. Conventional MAPS do not apply high voltages to the sensor to avoid interference with the readout electronics. Charge collection happens through diffusion, which is much slower (microseconds) than collection via drift (nanoseconds).

High-Voltage Monolithic Active Pixel Sensors High-Voltage Monolithic Active Pixel Sensors (HV-MAPS) are MAPS where a high voltage is applied to achieve a faster charge collection via drift. To shield the electronics from the high voltage and electric field the electronics are placed on a deep n-well within a p-substrate. The concept is shown in Figure 1.13. The sensor can be thinned down to the depletion zone to decrease the amount of material further.

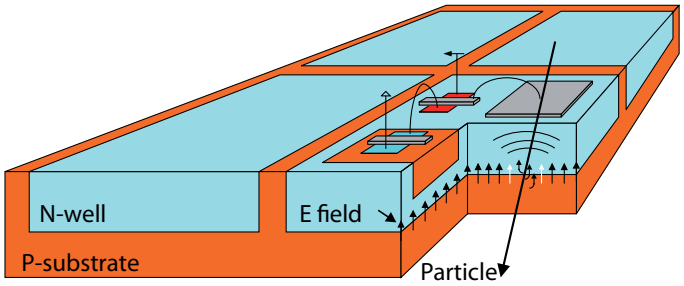

Figure 1.13: Concept of HV-MAPS. Taken from [18].

1.7.2 Charge Sharing

Charge sharing occurs when the deposited charges from one traversing particle are split and collected by different pixel diodes. Charge sharing can for example happen when via lateral diffusion close to the border between two adjacent pixels (Figure 1.14a) or when a particle traverses with a shallow incidence angle (Figure 1.14b).
The pixel hits that are created from a single particle are called clusters and the number of pixels in the cluster is called cluster size. The distribution of the cluster size strongly depends the properties of the sensor. For example, reducing the pixel size results in larger clusters and increasing the electric field strength results in smaller clusters.

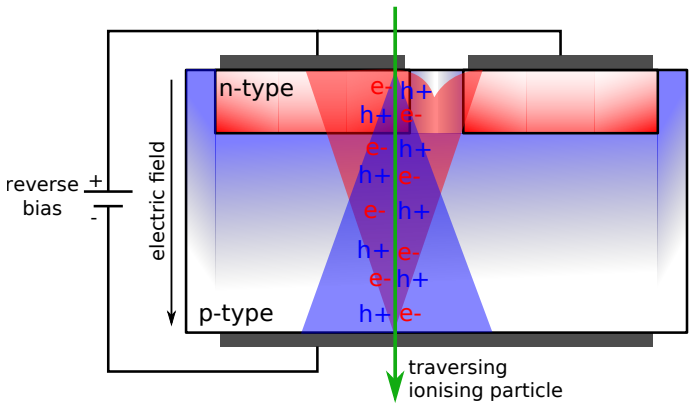

(a) Charge sharing created via lateral diffusion. Taken from [19].

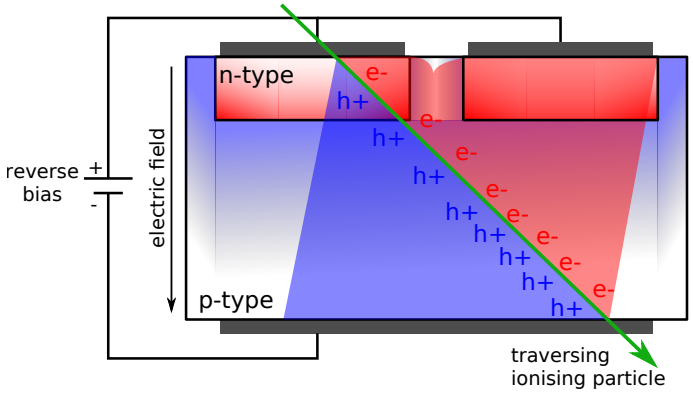

(b) Charge sharing from shallow incidence angle. Taken from [19].

Figure 1.14: Charge sharing in pixel sensors.

1.8 Monte Carlo Simulations

Monte Carlo (MC) simulations are built to solve complex problems numerically using stochastic properties of the system. A simple example of a MC simulation is an approximation of π [20]. For this points are generated with random positions in a unit square. A quarter unit circle is drawn into the square emerging from one corner of the square. The area of this quarter circle is $\frac{\pi}{4}$. Since the area of the quarter circle can be approximated using the amount of points within the circle divided by the total amount of points in the square, π can be evaluated. The approximation approaches the true value the more points are created.

1.8.1 Geant4

Geant4 [21, 22, 23] is a MC simulation toolkit to reproduce interactions between particles and matter. It has a wide range of applications, for example in High Energy Physics (HEP) to simulate the outcome of particle collisions or in medical research to simulate the absorption of radiation in different body tissues.
In Geant4 the detector geometry is defined by volumes with a certain material. The simulation is event based. An event could for example start with a single electron moving in a specific direction. The movement of the particle is then simulated in steps. Geant4 can also simulate the decay of particles or scattering with material, while keeping the MC truth information. This means that particles that are for example created by scattering processes can be traced back to the parent particle that was responsible for their creation. Geant4 version 10.7.1 was used in this thesis.

1.8.2 ROOT

ROOT [24, 25] is a data analysis framework that is widely used in HEP. Thanks to its speed and large feature set, it is also commonly used in MC simulations such as Geant4. One class is particularly useful for MC simulations, the `TTree` class. It works similar to a table or spreadsheet, it can store entries with flexible columns. The columns of a `TTree` can be filtered by complex expression. An example for such a use case would be different particles traversing a detector. If the `TTree` has a column for the particle ID, the end result can be filtered easily for different particles.
Besides its use for data structures, ROOT has also tools for fitting and data visualization. ROOT version 6.24.02 was used in this thesis.

1.8.3 Allpix Squared

Allpix^2 [26, 27] is a generic pixel detector simulation framework. It uses Geant4 to simulate particles passing through the detector, but extends it with a modular system for different kinds of pixel detectors and various physics models for a faster simulation speed.
The simulation chain is split in four major steps: generation of the deposited charges, propagation of the deposited charge inside the pixel, transfer of the propagated charges to the electronics and finally the digitization of the hit.
The modules and settings used in this thesis are described later in detail in section 4.1.
For this thesis, a modified version of Allpix^2 has been developed starting from version 2.0.1 released in July 2021. The final version used was rebased against Allpix^2 git commit `3c61e991`, for more details see section 4.2.

Chapter 2

Setup

2.1 MuPix10

The MuPix chips are a series of HV-MAPS developed for the Mu3e experiment. The MuPix10 is the first sensor to fulfill all technical design specification of the Mu3e experiment [7]. It is manufactured in the 180 nm HV-CMOS process from TSI Semiconductors.
The chip has a total size of 20.66 mm × 23.18 mm (Figure 2.1), with an active area of 20.48 mm × 20.00 mm. The sensor consists of a 256 × 250 pixel matrix, where each pixel has a size of 80 µm × 80 µm. The pixels have a deep n-well as charge collection diode, which is placed in the p-substrate that is connected to the high-voltage. The pixel matrix

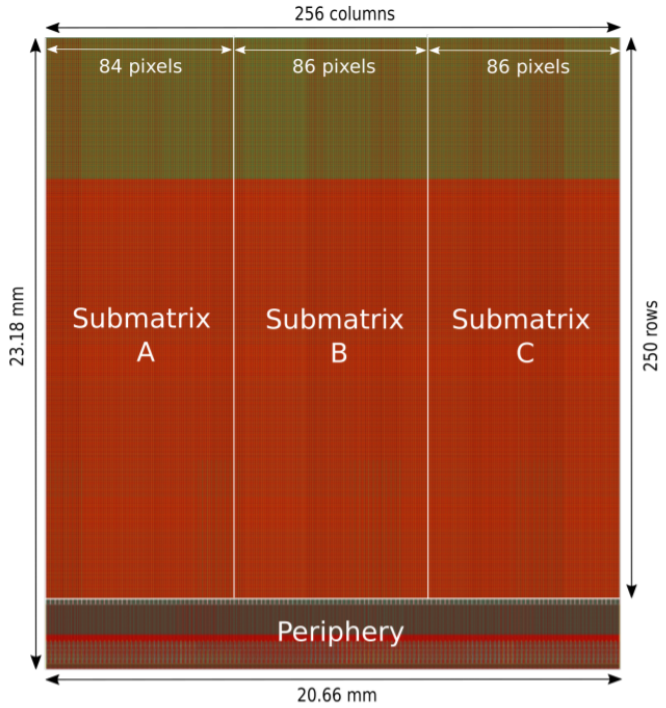

Figure 2.1: Layout of the MuPix10. Taken from [28].

is divided into three submatrices. Placed below the active area is the chip periphery. Inside each pixel in the active area is an amplifier, whose output is driven to a partner pixel in

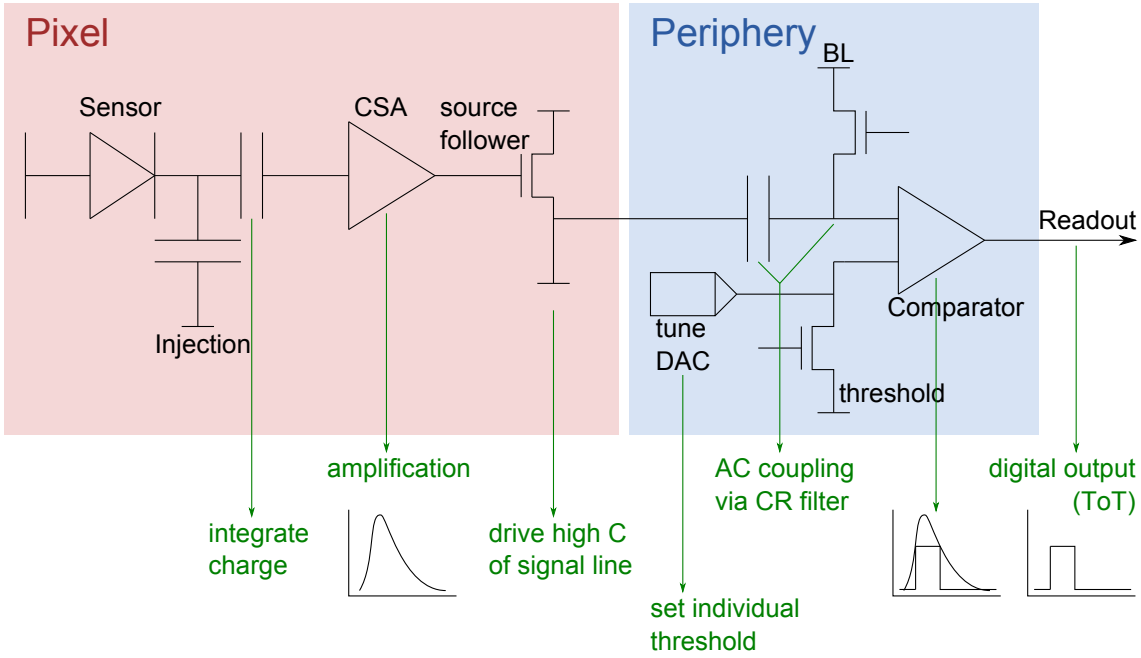

Figure 2.2: Periphery of the MuPix10 [6].

the periphery. Here the output of the amplifier is compared with a per-pixel adjustable threshold. The comparator output is then passed to a state machine, which sends data out via LVDS. Figure 2.2 gives a simplified overview of the periphery.
The reference clock of the chip runs at 125 MHz, providing a bandwidth of 1.25 Gbit/s for each LVDS link, one per submatrix. Using the three links individually, theoretically a hit rate of 90 MHit/s can be transmitted [29].

2.1.1 Analog Cell

The analog cell of the MuPix10 is inside each pixel and its goal is to amplify the charge collected from a traversing particle to a voltage pulse. This task is performed by a Charge Sensitive Amplifier (CSA). The circuit has a negative feedback loop to discharge the capacitor, which reduces the occupancy to allow high rate measurements. The output of the amplifier is driven to the digital cell via a source follower. Figure 2.3 gives a simplified overview of the circuit.
The pulse shape can be controlled by several digital-to-analog converters (DACs):

- BLPix: Baseline voltage for signal transmission
- BLResPix: Resistivity for baseline restoration
- VNPix: Current source for the amplifier
- VNOutPix: Current source for signal transmission
- VNFollPix: Current source for feedback
- VNFBPix: Resistive amplifier feedback
- VPLoadPix: Conductive amplifier feedback

The impact of the DACs on the pulse shape is described in [30].

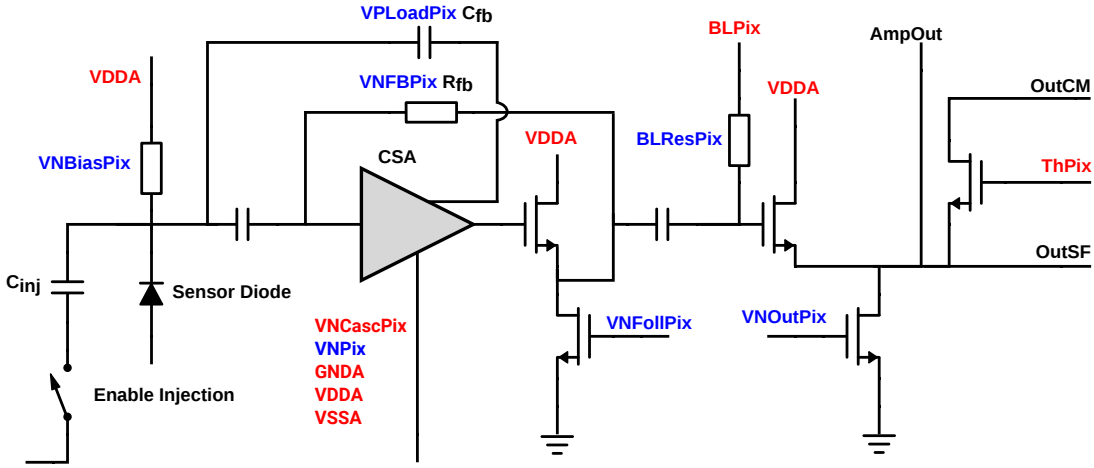

Figure 2.3: Schematic of the analog cell in the MuPix10. Taken from [30].

2.1.2 Digital Cell

To digitize the hit information, the output of the amplifier is compared to a given threshold. The time in which the amplified pulse is above this threshold is measured and referred to as ToT (Time-over-Threshold). The more charge is deposited in the sensor, the higher and longer the amplified pulse, which results in a longer ToT. Since the amount of deposited charges depends on the energy of the traversing particle, the ToT does as well.
In the MuPix10, an edge detector is connected to the output of the comparator. When the pulse crosses the threshold for the first time, a timestamp is stored, called TS1 or ToA (Time-of-Arrival). Similarly, a second timestamp, called TS2, is stored for the falling edge. TS1 is used to retrieve the time of the hit. The time delay between the initial signal response and the ToA is called Time-Walk. Since Time-Walk depends on the height of the pulse and affects the time resolution, TWC (Time-Walk Correction) needs to be done. This is done offline for the MuPix10.
The MuPix10 has two comparators with adjustable threshold levels to improve time resolution. In the Single Threshold Mode only one comparator is used. In the 2-Threshold

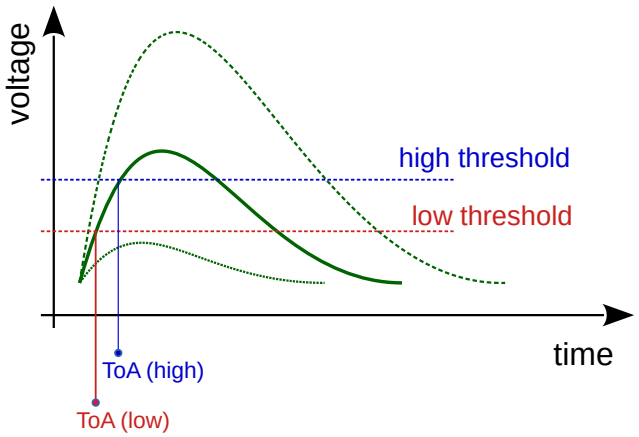

Figure 2.4: Concept of Time-over-Threshold measurements. Modified from [7].

Mode, one comparator is set close to the noise level and the other one to a higher value (see Figure 2.4). When the low threshold (ThLow) is crossed, its ToA timestamp is hold, but no hit flag is set. When the pulse crosses the high threshold (ThHigh), the hit flag gets set and TS2 is determined using ThHigh. If the pulse never crosses ThHigh, no hit flag is set. This allows for a ToT measurement closer to the noise level which decreases the impact of timewalk, without adding noise hits.
In this thesis, only the Single Threshold Mode is used. For testing purposes the output of the comparator, called Hitbus, can be routed out to a dedicated line where it can be read with an oscilloscope. A similarly routed output also exists for the output signal of the amplifier and is called AmpOut.
The precision of the timestamps also impacts the resolution of the ToA and ToT, and thus the time resolution. On the MuPix10, TS1 has a precision of 11 bit and TS2 of 5 bit. Their granularity can be controlled with clock dividers, steerable by the ckdivend (TS1) and ckdivend2 (TS2) DACs. TS1 is sampled every ckdivend + 1 clock cycles relative to the main clock, which is set to 125 MHz, and TS2 every ckdivend2 + 1 clock cycles. The default values are ckdivend = 0 and ckdivend2 = 15, which results in a binning of 8 ns for TS1 and 128 ns for TS2.
The chip also has a ToT cap. When a hit is registered, the readout is withhold and a capacity is charged with a constant current. Once the voltage of this capacity crosses a certain threshold, the readout is enabled again. This point in time determines the latest point when TS2 is stored, effectively capping the ToT to a certain value.

2.1.3 Injection

The MuPix10 has an injection circuit to introduce charge into the readout chain without requiring a real source. The circuit is shown in Figure 2.5. The injection capacity can be charged by applying an external voltage. When it discharges, it produces a current that flows into the CSA, which mimics a charge input from the sensor diode.

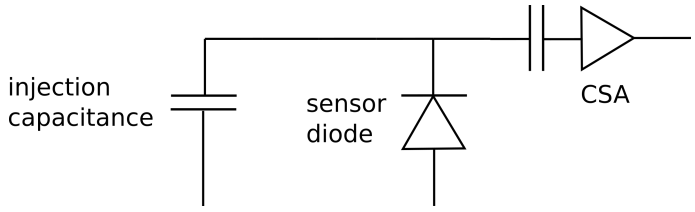

Figure 2.5: Circuit Diagram for the Injection. Taken from [28].

The charge that gets injected can be calculated from the injection voltage with Equation 2.1.

$$Q_{\text{inj}} = C_{\text{inj}} \cdot U_{\text{inj}} \tag{2.1}$$

2.2 Insert and Motherboard

For measurements in the lab the MuPix10 sensors are bonded to a Printed Circuit Board (PCB) called the MuPix10 insert (Figure 2.6). The insert connects power and data lines to the chip. It also provides test points for various voltages to perform direct measurements of the internal DACs and thresholds. The insert can be connected to a MuPix10 motherboard

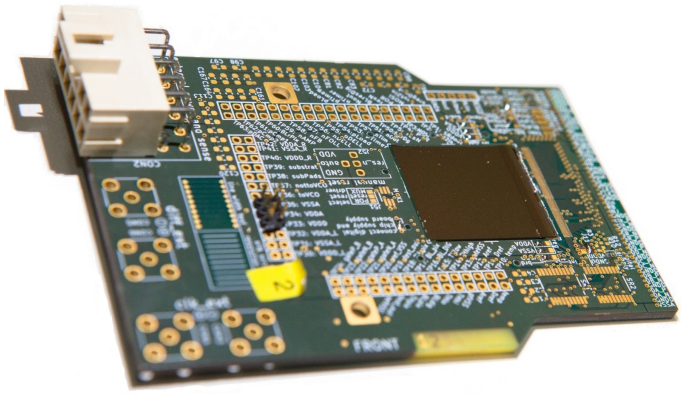

Figure 2.6: MuPix10 insert with bonded sensor [6]. The connector on the left side connects external VDD, VDDA and VSSA to the chip.

(Figure 2.7) via an edge connector. The motherboard generates voltages and clocks for the chip. It connects the data lines of the chip to an FPGA via a SCSI III connector. There are two LEMO connectors on the motherboard, which allow to measure the injection signal and the Hitbus.

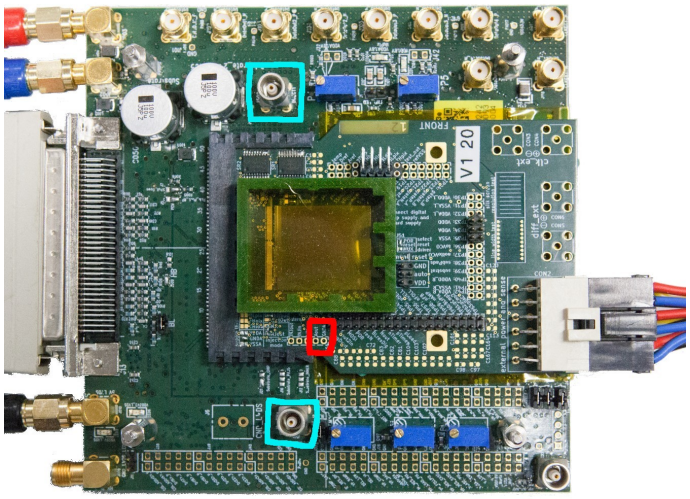

Figure 2.7: MuPix10 insert with motherboard [6]. Test outputs: AmpOut (red, on insert), Hitbus (cyan, below the insert) and Injection (cyan, above the insert). The cable on the top left connects to the HV, the cables next to the SCSI connector provide 5 V to operate the motherboard, the cable on the right provides the voltages to operate the MuPix10.

2.3 DAQ

The data acquisition system (DAQ) consists of an FPGA connected to a computer running the data acquisition software. A Field Programmable Gate Array (FPGA) is an integrated circuit that allows programming digital circuits. It is used to send the input signals for the chip configuration and to read the serialized data from the MuPix10. The software used is the MuPix Telescope DAQ software, which is described in [31].

2.4 Oscilloscope

The waveforms of Injection, AmpOut and Hitbus are measured using a Tektronix DPO 7245C digital oscilloscope [32]. The horizontal resolution is set to 100 MSample/s. The outputs are terminated with 1 MΩ. High frequency noise is filtered on all signals with a 20 MHz bandwidth filter. Injection and Hitbus are measured with DC coupling, the AmpOut is measured with AC coupling to remove any DC offset when triggering on the channel.
Screenshots from the oscilloscope of measured waveforms are shown in Figure 2.8.

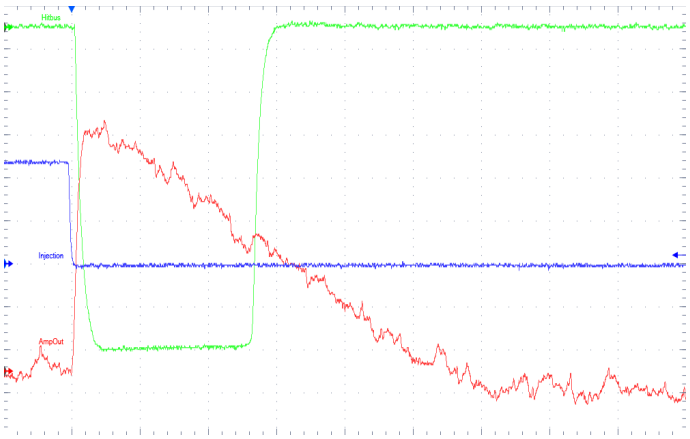

(a) Single pulse.

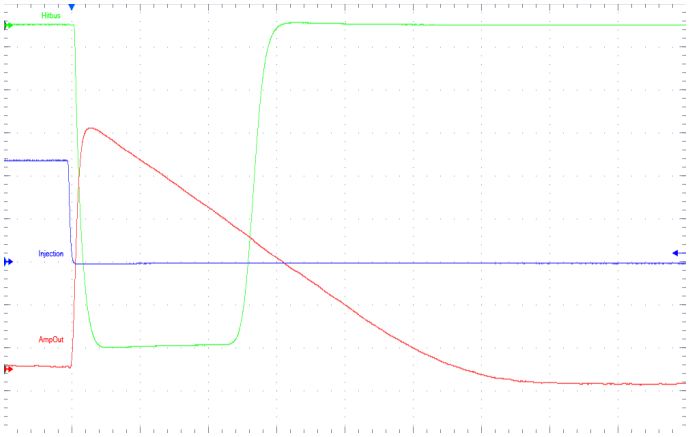

(b) Average of 500 pulses.

Figure 2.8: Waveform measurements on oscilloscope for 500 mV injection. AmpOut in red, Hitbus in green and the injection signal in blue. Horizontal scale 1.5 µs per division. Vertical scale for the AmpOut 30 mV per division.

2.5 Radioactive Sources

In this thesis ^{55}Fe (Iron-55, Fe55) and ^{90}Sr (Strontium-90, Sr90) were used as radioactive sources for different purposes. The last measured activity of the sources is given in Table 2.1.

Source	Label	Activity	Date
Iron-55	RK441	332 MBq	2020-01-08
Strontium-90	AE9773	7.4 MBq	2020-01-08

Table 2.1: Activity of the used radioactive sources.

2.5.1 Iron-55

^{55}Fe [33] decays into ^{55}Mn (Manganese-55) via electron capture with a half-life of 2.737 yr. After the decay, an electron from a higher shell fills the vacant spot in the K shell.
About 60 % of the time an Auger electron with an energy of 5.19 keV is emitted. Given its low energy, the probability that the electron leaves the source is negligible.
On the other hand, photon emissions for the $K_{\alpha 1}$ and $K_{\alpha 2}$ transmission line with energies of 5.898 75 keV and 5.887 65 keV have probabilities of 16.2 % and 8.2 %. Since the energy difference is lower than the energy resolution of most semiconductor detectors, they are often treated as a combined 5.9 keV line.
The K_β transmission line has a energy of 6.490 45 keV with a probability of 2.85 %.
Other minor decay modes contribute to the decay line, such as lower energy Auger electrons and other photon transmission lines.

2.5.2 Strontium-90

^{90}Sr [34] undergoes a β^- decay into ^{90}Y (Yttrium-90, Y90) with a half-life of 28.8 yr.
The decay energy of 0.546 MeV is split by the electron, the antineutrino and the ^{90}Y isotope. ^{90}Y itself also decays via β^- into the stable ^{90}Zr (Zirconium-90) isotope. The half-life of this decay is 64 h and the decay energy is 2.28 MeV.
The energy of the electrons from a ^{90}Sr decay is quite low, usually between 200 keV and 400 keV. As a result they can already be absorbed in the source, reducing the effective amount of low-energy electrons emitted from the source. Since ^{90}Y also emits electrons in this energy region, the energy spectrum of a real ^{90}Sr source can be assumed to only slightly deviate from the spectrum of a ^{90}Y source.

Chapter 3

Measurements

3.1 AmpOut Waveforms

For each injection voltage 5000 waveforms have been recorded. The measurements were triggered on the injection signal, so that each waveform has the same time offset. Tables with the used chip model, settings and voltages are give in Appendix A. The default DAC settings for the MuPix10 have been used (Table A.5).
In Figure 3.1 the average waveform for each injection is shown. For pulses above 800 mV injection, saturation effects are visible. For pulses that hit saturation the amplitude increases less with the injection voltage and the fall rate is not linear at the beginning of the falling edge.

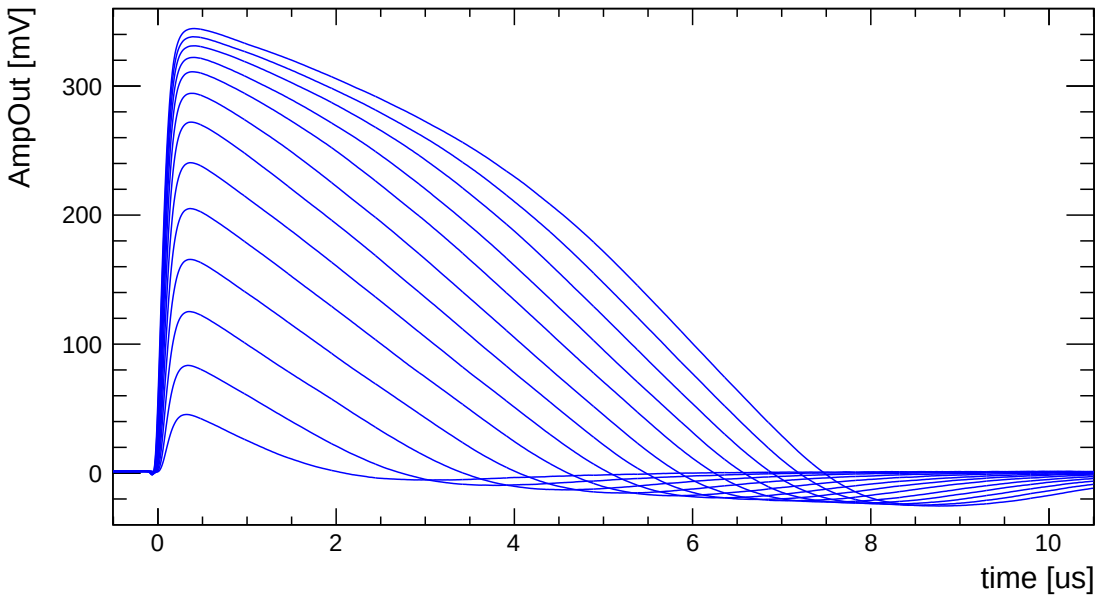

Figure 3.1: Average AmpOut waveforms for various injection voltages. Ranging from 200 mV injection for the smallest pulse up to 1.4 V for the largest pulse in steps of 100 mV.

The noise level, consisting of noise from the amplifier itself and from the signal transport, was estimated to be about 5 mV using the standard deviation in the average waveforms. The vertical uncertainty of the oscilloscope is assumed to be negligible in comparison.

3.2 Waveform Fitting

In this section the output waveform is described empirically and a fit function is built. As seen in Figure 3.1, the waveforms have a steep rise before they fall linearly. It was observed, that the falling slope is not constant across the injection voltages. To accommodate for this the base shape was described as a RC shaper [35]. It is given in Equation 3.1, the parameters are described in Table 3.1.

$$U_{\text{base}}(t) = A\left(\exp\left(-\frac{t}{t_F}\right) - \exp\left(-\frac{t}{t_R}\right)\right) \tag{3.1}$$

To help the fitting algorithms, the discontinuity at $t = 0$ was smoothed with an exponential. The adjusted base shape is given in Equation 3.2.

$$U_{\text{base, smoothed}}(t) = U_{\text{base}}(t)\left(1 - \exp\left(-\frac{t}{t_S}\right)\right) \tag{3.2}$$

A quasi-constant feedback is applied to the pulse. This means, that the feedback decreases exponentially for small signals ($< 10\,\text{mV}$) to model the decreasing fall rate observed when the signal is close to the baseline. The relation is given in Equation 3.3.

$$\dot{U}_{Fb}(U_{\text{signal}}) = Fb\left(1 - \exp\left(-\frac{U_{\text{signal}}}{Fb_D}\right)\right) \tag{3.3}$$

The signal is integrated over time, meaning that the signal in the next time step is calculated from the current signal. In every time step the difference in the base shape is added and then the feedback is applied to give the new signal. In Equation 3.4 the process is described mathematically for one time step.

$$\begin{aligned} U_{\text{basediff}}(t + \Delta t) &= U_{\text{base, smoothed}}(t + \Delta t) - U_{\text{base, smoothed}}(t) \\ U_{\text{pre}Fb}(t + \Delta t) &= U_{\text{signal}}(t) + U_{\text{basediff}}(t + \Delta t) \\ U_{\text{signal}}(t + \Delta t) &= U_{\text{pre}Fb}(t + \Delta t) - \dot{U}_{Fb}\big(U_{\text{pre}Fb}\,(t + \Delta t)\big) \cdot \Delta t \end{aligned} \tag{3.4}$$

Finally saturation is applied to the output. This only done once at the end for the final result and does not influence the integration. The saturation is modeled with the logistic function and given in Equation 3.5.

$$U_{\text{signal, saturated}}\big(U_{\text{signal}}\big) = U_{\text{sat}}\left(\frac{2}{1 + \exp\left(-2\frac{U_{\text{signal}}}{U_{\text{sat}}}\right)} - 1\right) \tag{3.5}$$

In Appendix B is an implementation of the fit function in C++ for fitting with ROOT. It was observed that many of the parameters have a direct correlation, for example t_F and Fb. Fitting with this function also provided some difficulties when all parameters are free due to precision issues. In the end a fixed parameter set was chosen based on tests with varying amounts of free parameters that works within a large region of input signals. The parameters are given in Table 3.1. For the final fit, only the time offset of the waveform and the amplification parameter were free. The fitting procedure for the final fit is also described in Appendix B.

Parameter	Description	Value
A	Amplification parameter	charge dependent
t_R	Rise time RC shaper	0.1 µs
t_F	Fall time RC shaper	4.8 µs
t_S	Rising edge smoothing time	0.1 µs
Fb	Feedback rate	23 mV/µs
Fb_D	Feedback damping parameter	2 mV
U_{sat}	Saturation voltage	360 mV

Table 3.1: Pulse shape parameters.

In Figure 3.2 the fit (red) for the average waveform for 500 mV injection (blue) is shown. The error on the waveform is the standard deviation from the combination of the averages. Appendix C contains the results of all fits.
Overall the function and parameter give a good result that lies within the error of the waveform. The fit gets worse for small signals such as 200 mV injection and large signals such as 1.4 V injection. A χ^2_{red} value is not given here, as the errors on the function mostly come from noise of the signal, and thus is unrealistically low, often much smaller than 1. More relevant in this case is the deviation between the data and the fit in the relevant threshold level. This level in between 10 mV and 50 mV, depending on the settings. For 200 mV the difference is less than one TS2 bin (128 ns). Even for very large pulses such as 1.4 V the difference is not larger than at most two TS2 bins, even though the fit fails to lie within the noise level at all times.

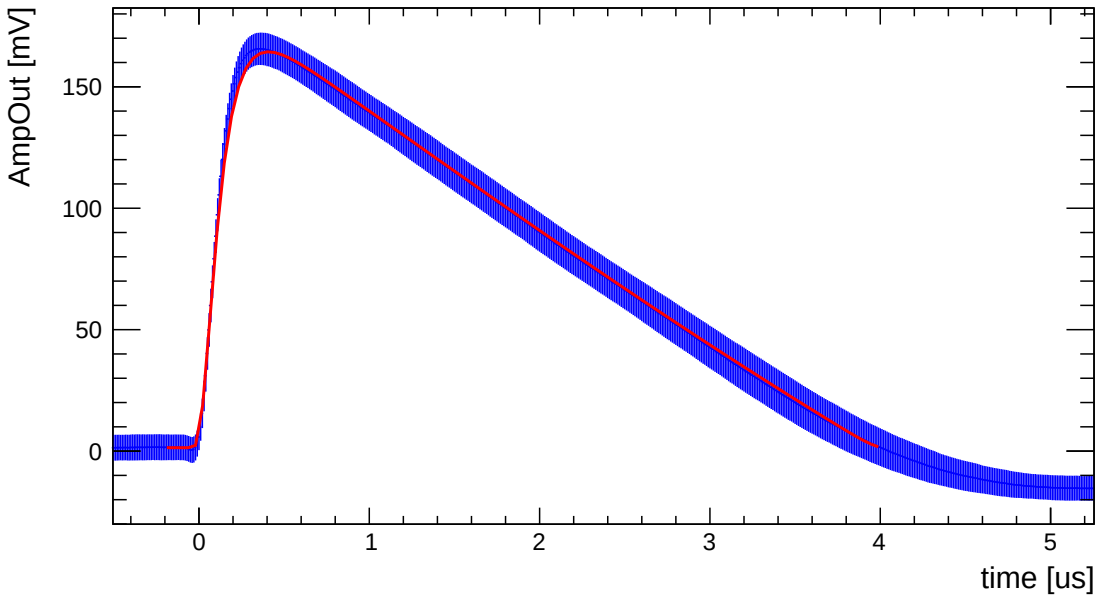

Figure 3.2: Average pulse waveform for 500 mV injection (blue) and fit (red). The fitted amplification parameter is (208.77 ± 0.66) mV. The error on the waveform is the standard deviation from the average and about 5 mV.

3.3 Injection Dependence

In this section, the dependency of the amplification parameter on the injection voltage is discussed. In Figure 3.3 the results from the pulse fits (Appendix C) are plotted in blue as function of the injection voltage.
For injection voltages above 300 mV, a linear dependency is found. However for small injections, this is not the case anymore. Here, the amplitude increases less with additional charge compared to higher injection voltages.

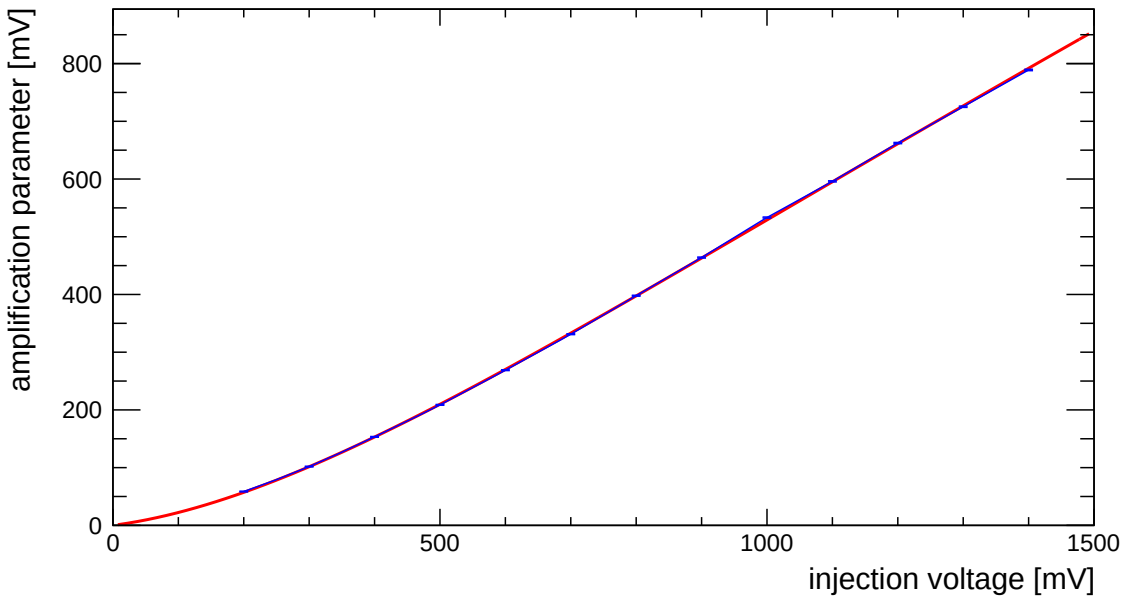

Figure 3.3: Fit results of the pulse amplification parameter plotted against the injection voltage. In blue are the data points for the injection pulse fits with an error in A (barely visible). The fit of the dependency is plotted in red.

To model this behavior, a linear function multiplied with an exponential fall for small voltages was used. The model also gives no amplification when nothing is injected, which is a useful property when using the model in simulations. It is given in Equation 3.6.

$$A(U_{\text{inj}}) = (A_{m,\,\text{inj}} \cdot U_{\text{inj}} + A_{c,\,\text{inj}}) \cdot \left(1 - \exp\left(-\frac{U_{\text{inj}}}{A_{\mu,\,\text{inj}}}\right)\right) \tag{3.6}$$

The fit is drawn in red into Figure 3.3. The fit results are given in Table 3.2.

Parameter	Value	Unit
$A_{m,\,\text{inj}}$	0.5624 ± 0.0011	1
$A_{c,\,\text{inj}}$	87.6 ± 4.3	mV
$A_{\mu,\,\text{inj}}$	595 ± 11	mV

Table 3.2: Fitted parameters for the amplification-injection dependency.

3.4 Injection Calibration

Since the injection capacity can vary widely between different pixels, a calibration has to be done to convert the injection voltage to the injected charge. There are several sophisticated methods to do this, e.g. [36], however in this section a simple approach is described using a single calibration point.
For the pulse shape described in section 3.2 and the dependency of the amplification parameter A given in section 3.3, the following concept was used for calibration.
Given a calibration point, that means a point where the amplification parameter A_{cal} is given for a known charge input Q_{cal}, it can be determined where this point is on the amplification-injection dependency curve, giving an equivalent injection voltage U_{cal}. The injection capacity is then given by Equation 3.7.

$$C_{\text{inj}} = \frac{Q_{\text{cal}}}{U_{\text{cal}}} \tag{3.7}$$

The calibration point can be obtained by using a monochromatic photon source. For the MuPix10, ^{55}Fe (subsection 2.5.1) is a feasible option due to its almost monochromatic X-rays that inject charges within the working range of the amplifier. While ^{55}Fe emits both photons on the K_α line and on the K_β line, the difference between these is small enough that it falls below the energy resolution of the MuPix10.
The value used for Q_{cal} is $(1605 \pm 14)\,\text{e}$. This value will be derived later in section 4.3 using a Monte Carlo simulation.
Determining U_{cal} from A_{cal} is done numerically as Equation 3.6 is not trivially solvable. To get an estimate of the error of U_{cal}, it was determined numerically multiple times with the errors applied to the parameters. With $(91.2 \pm 1.1)\,\text{mV}$ for A_{cal} (Appendix C), U_{cal} was calculated to be $(278.2 \pm 8.9)\,\text{mV}$.
With these value the injection capacity is $C_{\text{inj}} = (0.924 \pm 0.031)\,\text{fF}$, which is within the design specification of 0.75 fF to 1 fF and is similar to the value found for the MuPix8 [30].

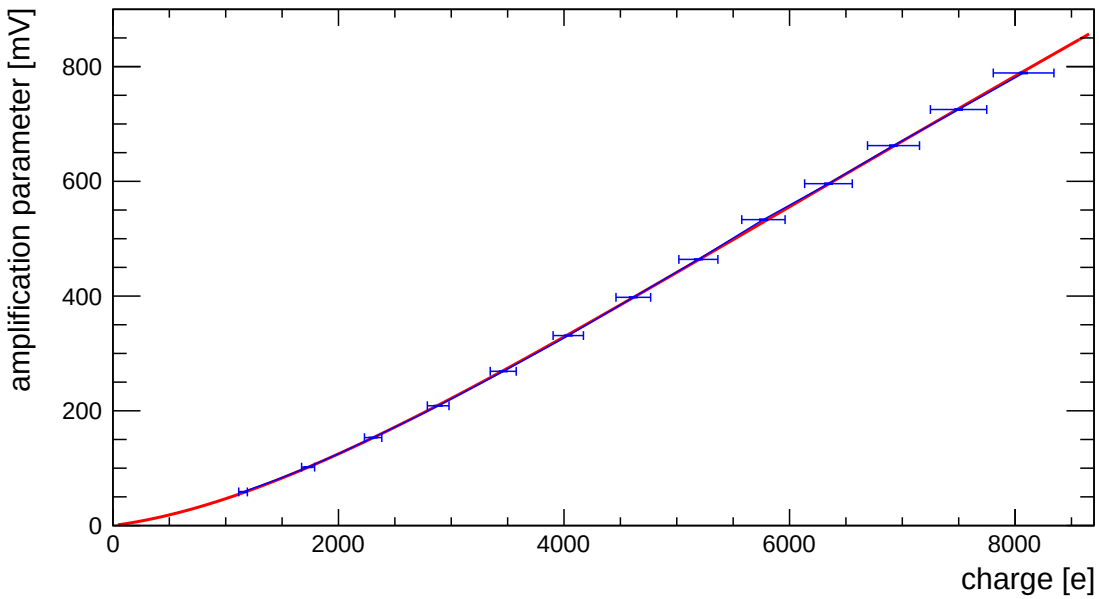

Figure 3.4: Fit results of the pulse amplification parameter A plotted against the injected charge. Figure 3.3 converted to charge using the injection capacity.

The amplification parameter can be described for a given input charge as done in Equation 3.8.

$$A(Q) = (A_m \cdot Q + A_c) \cdot \left(1 - \exp\left(-\frac{Q}{A_\mu}\right)\right) \tag{3.8}$$

The parameters given in Table 3.3 are converted from Table 3.2 using Equation 2.1 and the determined value of the injection capacity.

Parameter	Conversion	Value	Unit
A_m	$A_{m,\,\mathrm{inj}}/C_{\mathrm{inj}}$	0.0975 ± 0.0033	mV/e
A_c	$A_{c,\,\mathrm{inj}}$	87.6 ± 4.3	mV
A_μ	$A_{\mu,\,\mathrm{inj}} \cdot C_{\mathrm{inj}}$	3.43 ± 0.13	ke

Table 3.3: Converted parameters for the amplification-charge dependency.

Figure 3.4 shows the dependency of the amplification parameter A on the injected charge. It is Figure 3.3 with the injection voltage converted to charge using Equation 2.1. The parameters of the curve are those given in Table 3.3.

It should be noted that the errors of the values, including the injection capacity, are underestimated. Due to the fixed parameters during the waveform fitting, the predicted error of A for each injection voltage is much smaller than if the parameters were not restricted. As this the fitting is a non-trivial issue, the errors up to this point should be taken more as guidelines than proper error bounds.

3.5 Strontium-90

Strontium-90 was measured in the lab with the DAQ. The source was placed about a centimeter above the sensor. The radiation hits the sensor from the frontside, where the metal line connections in the chip are placed.
In Figure 3.5 the Time-over-Threshold distribution is shown. The data has been analyzed for the entire sensor and for a single pixel. The pixel in column 120 and row 0 was chosen as it is the same pixel where the waveform measurements from section 3.1 have been done. The threshold level measured was 34 mV above the baseline (Appendix A, THlo − BLdig).

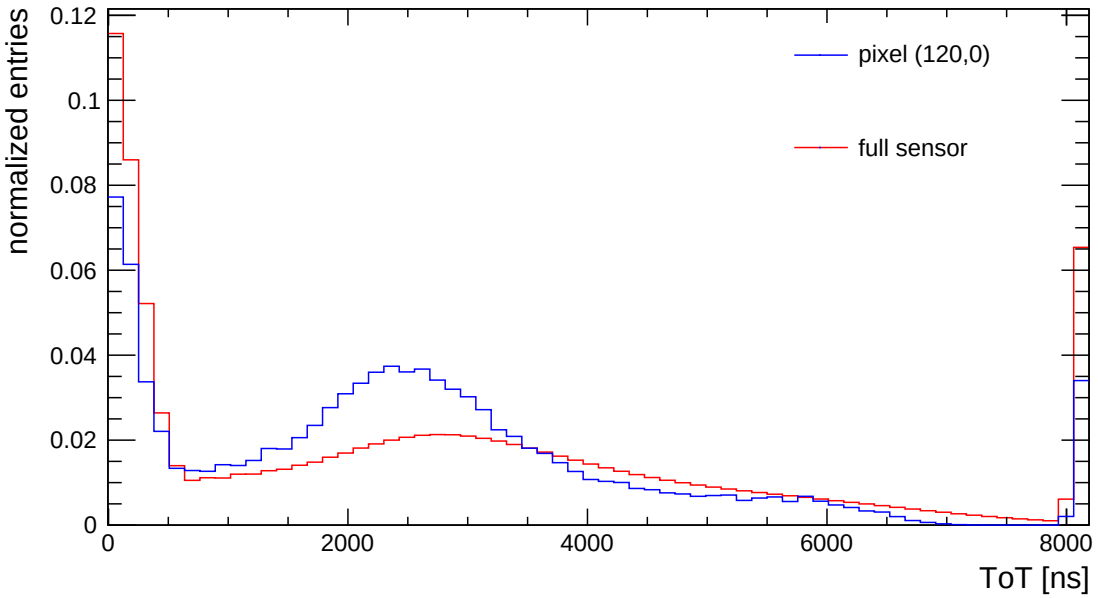

Figure 3.5: Measured ToT spectrum for ^{90}Sr.

The peak on the lower end of the spectra is due to noise and crosstalk between the pixels. Crosstalk occurs between adjacent signal lines due to capacitive coupling. When one line has a high signal, it is induced to the adjacent lines, although with a lower amplitude. This is why signals induced by crosstalk have a small ToT and the peak at the lower is seen. At the higher end of the spectrum the peak comes from miscalculations due to the internal clock of the timestamps.
To better compare the data, in Figure 3.6 the data is plotted with a cut for the ToT excluding values lower than 500 ns and higher than 8000 ns. It can be seen that the peaks between the entire sensor and the single pixel deviate. The peak of the entire sensor is at roughly 2800 ns, while the single pixel ToT peak is about 2500 ns. It was previously observed that the mean ToT for the same injection signal increases for pixels with higher row addresses [37]. This explains why the ToT for the entire sensor is higher than for the single pixel.
The variation in ToT between pixels can happen due to signal shaping in the transmission lines via capacitive coupling and variations during the manufacturing process. It was suggested that the variations might also come from power drops in the pixel matrix [37], but this is still being investigated.
In Figure 3.7 the cluster size distribution of the measurement with and without the ToT cut is given. It can be seen that the cut removes more entries with a cluster size of 2 as they are created from crosstalk.

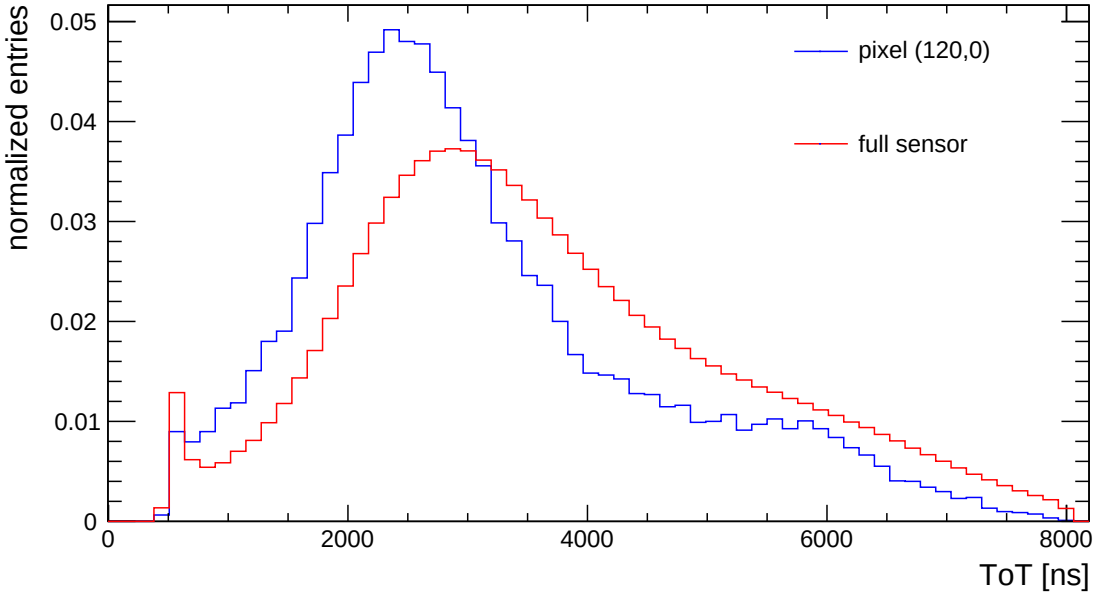

Figure 3.6: Measured ToT spectrum for ^{90}Sr. ToT > 500 ns and < 8000 ns.

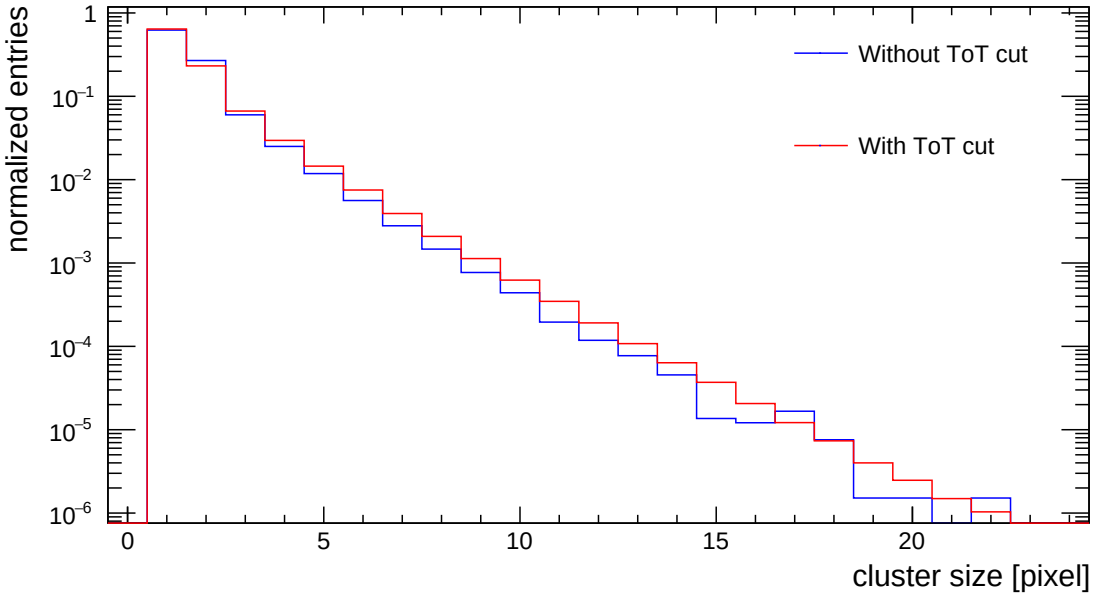

Figure 3.7: Measured cluster size distribution for ^{90}Sr. Comparison with ToT cut.

Chapter 4

Simulation

4.1 Physics Model

The model for the MuPix10 is a 100 µm thick chip operated at 100 V high-voltage in reverse bias. The estimated active sensor thickness is 85 µm with a 15 µm aluminum layer at the frontside of the sensor, accommodating for the line routing in the sensor. The implant size is set to 58 µm × 58 µm × 4 µm and placed on the frontside of the chip. Like in the lab incoming particles traverse the sensor from the frontside.
The electric field and doping concentration were extracted from a TCAD simulation of the MuPix10 pixel cell [38]. Cross sections of the electric field are shown in Figure 4.1. The field in the middle of the sensor decreases roughly linear in z-direction from the implant up to about 40 µm. At the edges of the pixel a high electric field is created by the highly p-doped guard ring. Its purpose is to reduce charge sharing between neighboring pixels.
While the chip used for the measurements had a thickness of 625 µm, the difference should be small considering that the electric field deeper than 50 µm is quite low and particles hit the sensor from the implant side. Using a thinner sensor has the advantage that its field can be computed much faster for the same resolution in the electric field.

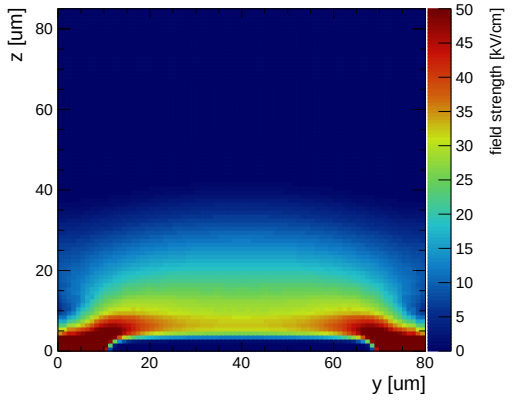

(a) Electric field in the yz plane cut in the middle of the sensor. The field strength scale was limited to better visualize the electric field in the sensor.

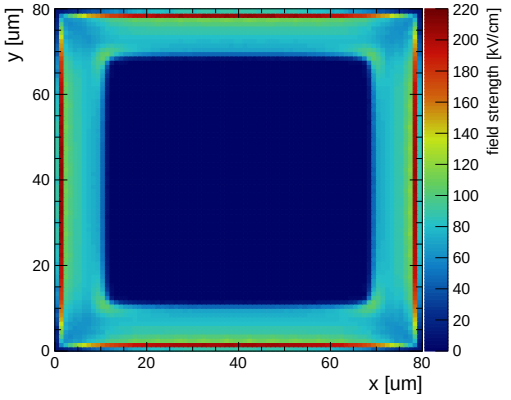

(b) Electric field in the xy plane cut at the implant. At the edges the effect of the highly p-doped pixel guard ring on the electric field is visible.

Figure 4.1: Electric fields in the MuPix10 pixel simulated using TCAD.

Geant4 is leveraged to simulate everything up to the charge deposition in the sensor using the `FTFP_BERT_LIV` physics list (see [23]). The Geant4 simulation chain starts with the initial source, for example an electron beam. In case of a radioactive source Geant4 simulate its decay. Geant4 then simulates the movements of particles in steps and their energy deposition per step, which is used later for the creation of electrons and holes. In this thesis the Geant4 simulation is created automatically using the built-in `DepositionGeant4` module of Allpix^2.
Allpix^2 offers several models for charge propagation within the sensor. In this thesis, the `GenericPropagation` module is used to simulate the propagation of the deposited charges. The temperature of the silicon is set to lab conditions (293 K), but it should be noted that the temperature of the chip might increase during operation.
For the charge carrier mobility model the Hamburg High-Field Model [39] was chosen. Hole propagation was enabled to include recombination effects. The model for charge carrier lifetime and recombination used is a combination based on the Shockley-Read-Hall (SRH) model [40, 41] and Auger recombination [42]. SRH recombination is also called trap-assisted recombination as it described the recombination of charge carriers with the lattice. The "traps" in the lattice are energy states, for example created by a dopant. Auger recombination describes the process when an electron and a hole recombine and the released energy is given to an electron or a hole in the same energy band.
The `PulseTransfer` module is used to collect and transfer the propagated charges to the digitizer. The charge pulses are binned in 0.1 ns bins for up to 1.5 ns.
In Figure 4.2 and Figure 4.3 the simulated movement of the charge carriers created from an electron with an energy of 1 MeV traversing the sensor at a 45° angle is shown. In Figure 4.2 the path of the traversing electron can be seen from the location of the created charge carriers. At a depth of $z \simeq 0.01$ mm, the separation of electrons and holes due to the electric field is visible. From this the depletion depth can be estimated to be around 40 µm. In this region electrons are attracted towards the implants, while holes move in the other direction. Outside the region, mobility through diffusion and recombination of charge carriers can be observed.
In Figure 4.3 the effect of charge sharing is visible. The electron traverses the sensor between pixel 127 and 128 in x-direction, and as a result the created electrons split and move towards different pixel implants. Further behind in y-direction, holes are moving towards the HV contact located at the vertex between the pixels.

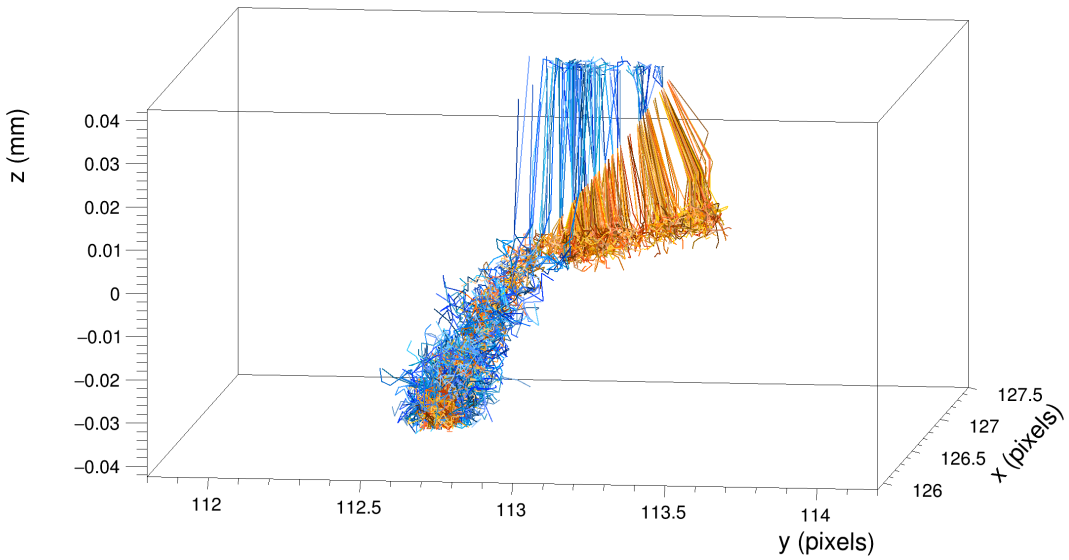

Figure 4.2: Simulated movement of charge carriers created from a 1 MeV electron traversing the sensor at a 45° angle. Electrons are colored in blue, holes in orange. The charge carrier separation effect of the depletion zone is visible.

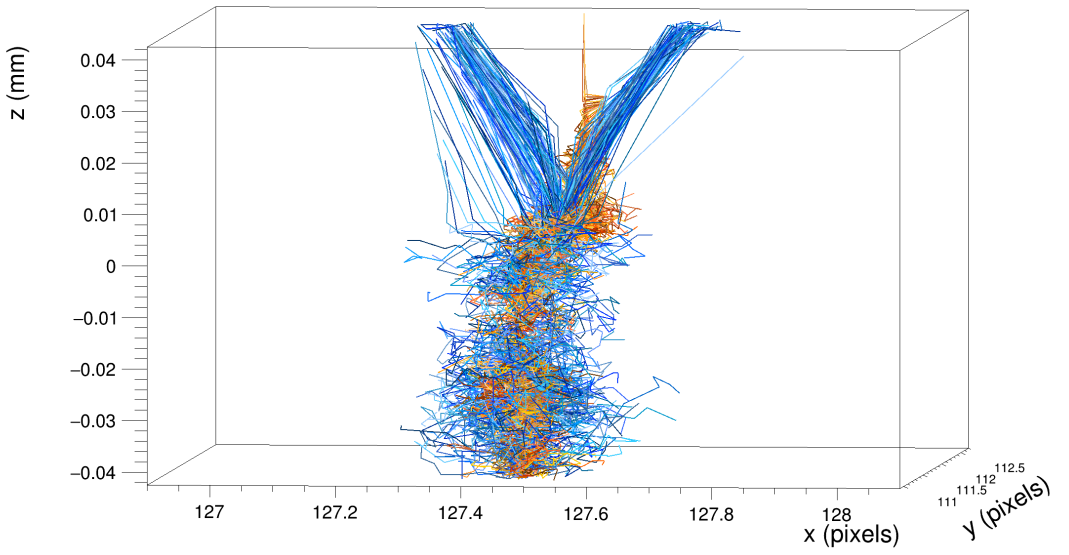

Figure 4.3: Simulated movement of charge carriers created from a 1 MeV electron traversing the sensor at a 45° angle. Electrons are colored in blue, holes in orange. Charge sharing between the pixels and holes moving to the HV contacts is visible.

4.2 MuPix Digitizer Module

To create digitized hits from the collected charges, there are two existing modules in Allpix^2: the `DefaultDigitizer` and `CSADigitizer` modules. The first generate an output signal via a linear charge-to-digital converter (QDC), which can give similar results as a ToT logic, but does not simulate one. The `CSADigitizer` features a charge-to-voltage-pulse amplification and determination of the ToA and ToT from that pulse. However, the CSA in the model has Krummenacher feedback [43], which results in a pulse shape that is different to the one in the MuPix10. The signal response in the module is proportional to the input charge, which also does not apply to the MuPix10.
For these reasons, a new module derived from the `CSADigitizer` was created for the MuPix10, the `MuPixDigitizer` module[1]. The pulse function described in section 3.2 is used with the relation for the amplification parameter found in section 3.3.
The amplification of the pulse starts at the time when the first input charge reaches the implant. From this time, the charge is integrated for 1 ns, with the rest of the pulse being ignored. This was done to only collect the fast charges created in the depletion zone, as few charges (per time) have less impact on the amplification, which was seen is in Figure 3.4. After the amplification, Gaussian noise is applied to every bin of the amplified pulse.
The limited charge integration simplification has been made as it was observed that the total amount of charge collected over a long time results in ToT spectrum noticeably higher than comparable measurements in the lab. A simulation that takes account of the timing for the incoming charges would go beyond the scope of this thesis. After inspection of several pulses with 1 MeV electrons it was found that about 1 ns after the initial incoming charge the peak from charge drift flattens.
In Figure 4.4 an example of a simulated charge pulse created from a 1 MeV electron is shown. In Figure 4.5 the corresponding amplified pulse with applied noise is shown. The charge integration begins at 0.1 ns and stops at at 1.1 ns. From the total charge of 3244 e the 1 ns interval covers 2957 e for amplification, which results in an amplification parameter that is roughly 12 % smaller than without the cut.
To determine TS1, the pulse is sampled every TS1 clock cycle, which is 8 ns in case of the MuPix10. The first TS1 clock cycle where the amplified pulse is above the threshold is used for the ToA.
TS2 is determined by the cycle where the last threshold crossing from above to below the threshold takes place. This simulates the edge detector after the comparator, from which the last edge is used for TS2. This process continues until the integration time or the ToT cap is reached. The ToT cap sets a maximum time after TS1 for TS2 and can be smeared with Gaussian noise to accommodate for variations in the manufacturing process.
The 2-Threshold and Ramp Mode of the MuPix10 are also implemented in the module, but will not be investigated in this thesis.

[1] The source code of the `MuPixDigitizer` module can be found at `https://github.com/stephanlachnit/allpix-squared/tree/p/mupix-digitizer`.

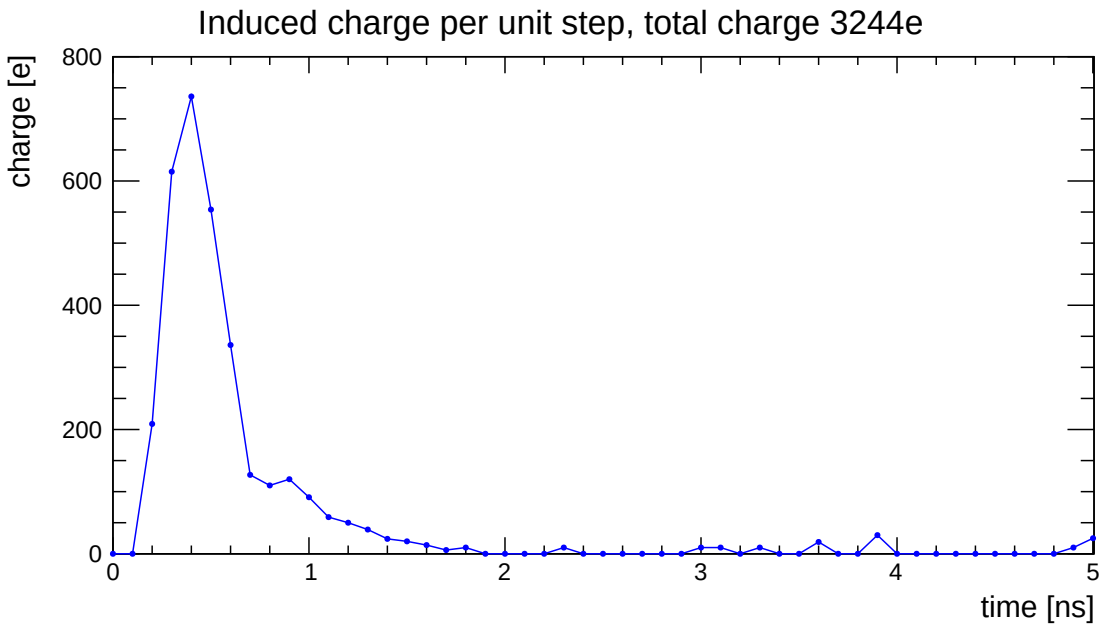

Figure 4.4: Simulated charge pulse created from a 1 MeV electron.

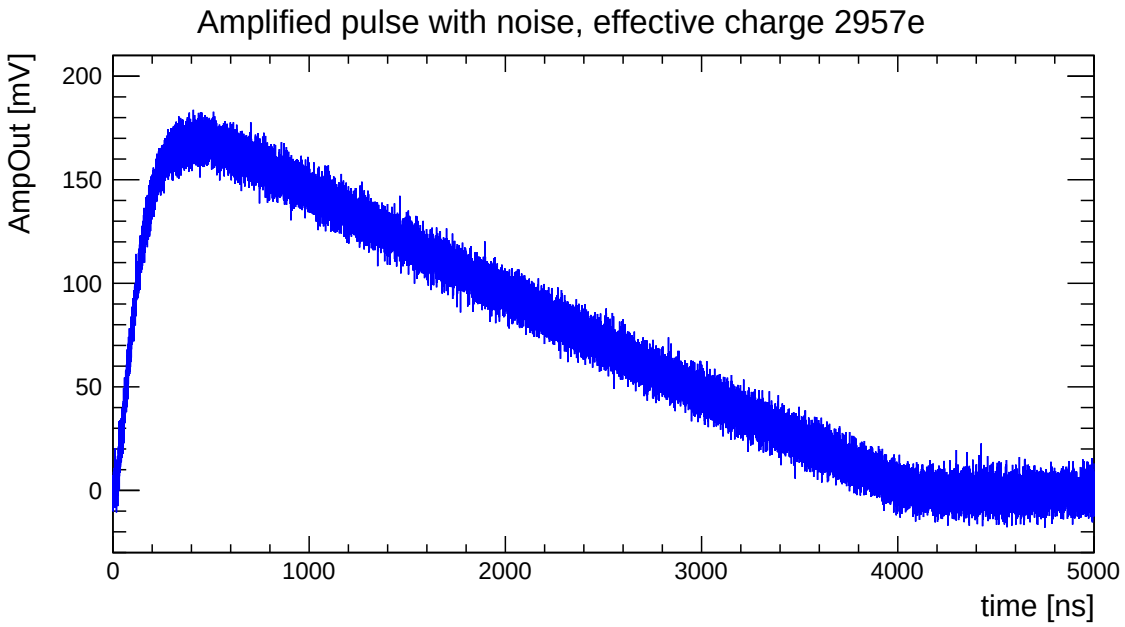

Figure 4.5: Simulated AmpOut pulse created from charge plot shown in Figure 4.4.

4.3 Iron-55 Charge Distribution

In this section the typical amount of collected charge from a ^{55}Fe source is derived. This value is used in section 3.4 for the injection calibration.
Using a classical approach, the amount of electrons a typical ^{55}Fe pulse creates can be calculated by hand. The energy of a typical ^{55}Fe has an energy of about 5.9 keV (subsection 2.5.1). The average creation energy for an electron-hole pair in silicon is about 3.64 eV (subsection 1.6.1). Assuming the photon is completely absorbed within the active material of the sensor and all energy goes into the creation of electron-hole pairs, the amount of created electron-hole pairs is given by Equation 4.1.

$$Q = \frac{5.9\,\mathrm{keV}}{3.64\,\mathrm{eV\,e^{-1}}} \simeq 1620\,\mathrm{e} \tag{4.1}$$

While this approach gives a good estimate, the charge distribution of ^{55}Fe can be generated using Allpix^2 for a more precise result. Since the simulation incorporates charge carrier lifetime and recombination, the expected value is lower than the previous calculation. Figure 4.6 shows the simulated charge distribution.

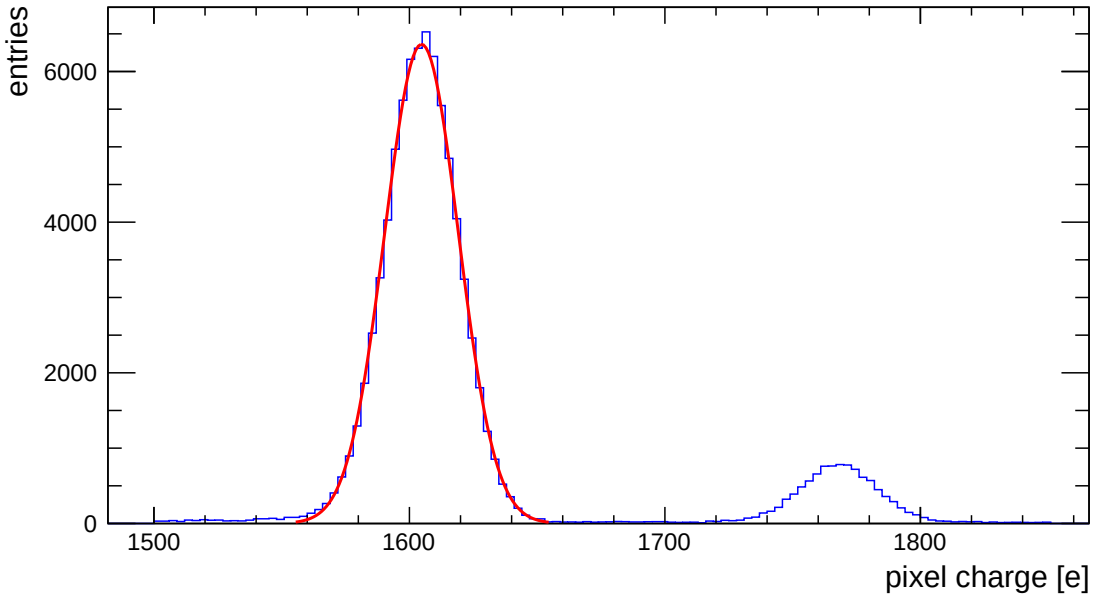

Figure 4.6: Simulated charge distribution for ^{55}Fe.

Two peak can be seen, a large one for the K_α lines and a smaller peak with more charge for the K_β line. Since the two peaks are so close that they can not be distinguished in the measurements, the K_α peak is used for the calibration. The final results from the Gaussian fit is $Q = (1605 \pm 14)\,\mathrm{e}$.

4.4 Strontium-90

A simulation was done to compare the model with the measurements from ^{90}Y. As already described in subsection 2.5.2, the electrons coming from the ^{90}Sr source can be modeled as being mostly the electrons from a ^{90}Y decay. For this thesis, 10 million ^{90}Y decays have been simulated for comparison with ^{90}Sr.

4.4.1 Charge

In Figure 4.7 the charge induced into a pixel plotted against the kinetic energy of the corresponding electron. This data is available thanks to the MC truth information in the simulation. The plot has two noteworthy features. For lower energy electrons, the amount of deposited charges increases. This is due to the Berger-Seltzer equation for energy loss of electrons and positrons discussed in subsection 1.5.2. The shape shows that electrons created by a ^{90}Y decay are mostly MIPs. For a better comparison to Figure 1.9, the plot is drawn with a logarithmic energy axis in Figure 4.8.
The second feature is the "noise" below the curve at low energies and low charges, which comes from charge sharing between pixels. In Figure 4.9 the total charge induced by a single electron is plotted against its energy. Comparing Figure 4.8 and Figure 4.9 shows that this feature vanishes when summing over the induced charges from a single particle.

4.4.2 ToT Spectrum

In Figure 4.11 the simulated ToT spectrum is compared to the measured ToT spectrum for a single pixel, in Figure 4.12 to the ToT spectrum for the entire sensor. The ToT histograms for the simulation have been cut with the same cut as for the measurement in section 3.5.
In the single pixel case the ToT peak of the simulation at about 2500 ns aligns with the measurement. For higher ToTs, the measurements drops faster than the simulation. Comparing the simulation with the spectrum for the entire sensor, the peak of the measurements is about 300 ns larger. As already discussed in section 3.5 this is due to the increasing mean ToT for rows with higher addresses. The spectrum of the entire sensor shows a behavior for large ToTs that is closer to the simulation than the single pixel measurement. This is likely due to the low statistics in the single pixel dataset. For a ToT larger than 7000 ns, the simulation shows more entries. This indicates that more electrons with a low energy traverse the sensor than in the measurement, which could be due to absorption of these electrons in the source.

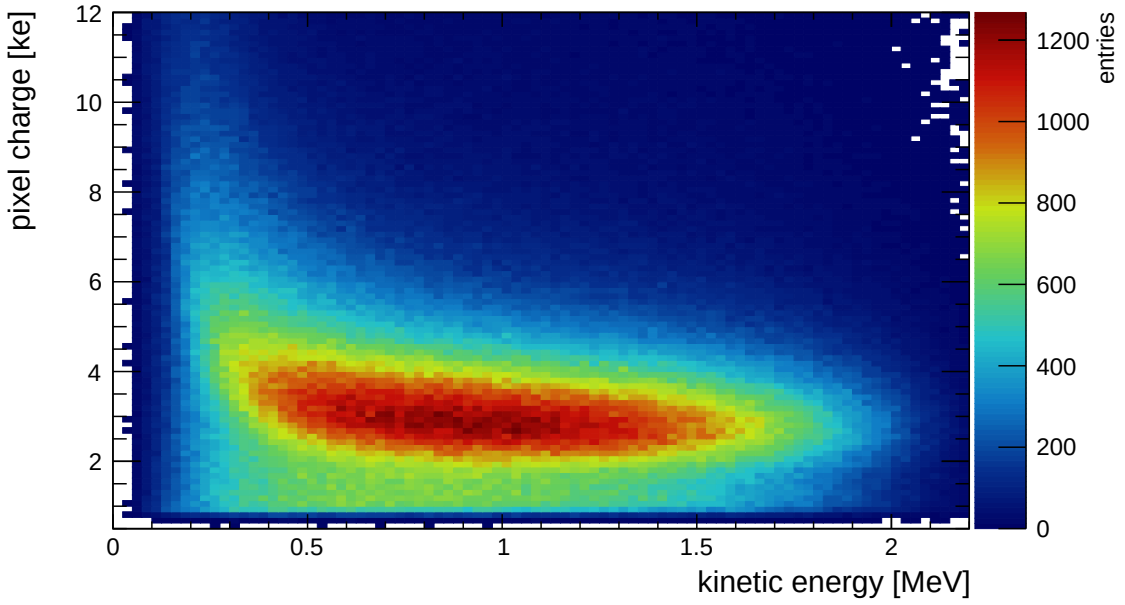

Figure 4.7: Charge induced into a pixel plotted against the kinetic energy of the corresponding electron. Data from the ^{90}Y simulation. The pixel charge range is limited for better visibility.

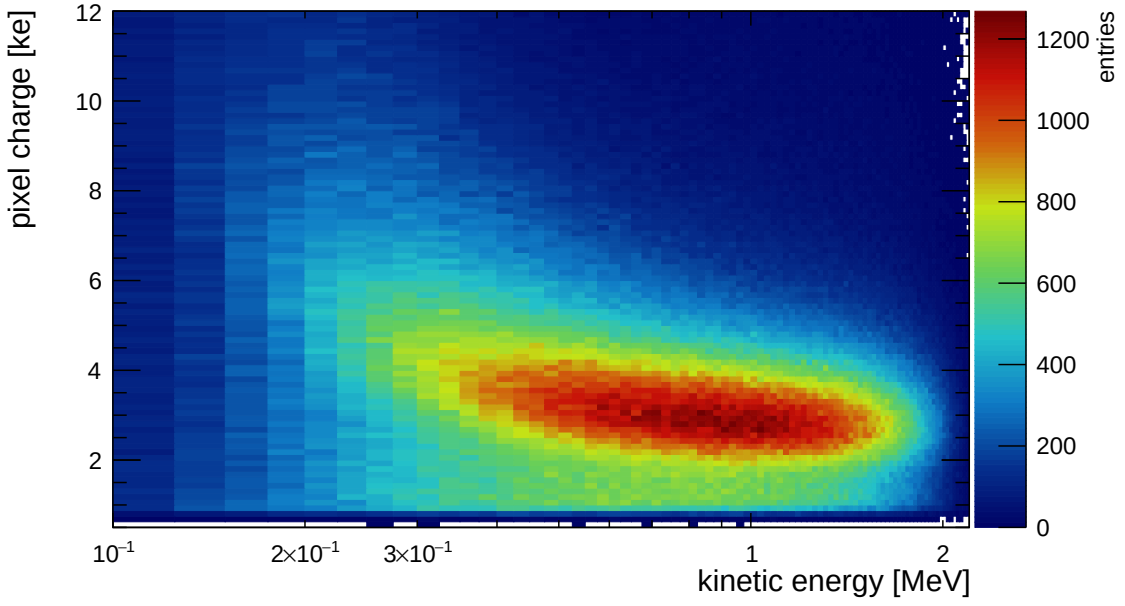

Figure 4.8: Charge induced into a pixel plotted against the kinetic energy of the corresponding electron. Data from the ^{90}Y simulation. Plotted with linear energy binning on logarithmic axis. The pixel charge range is limited for better visibility.

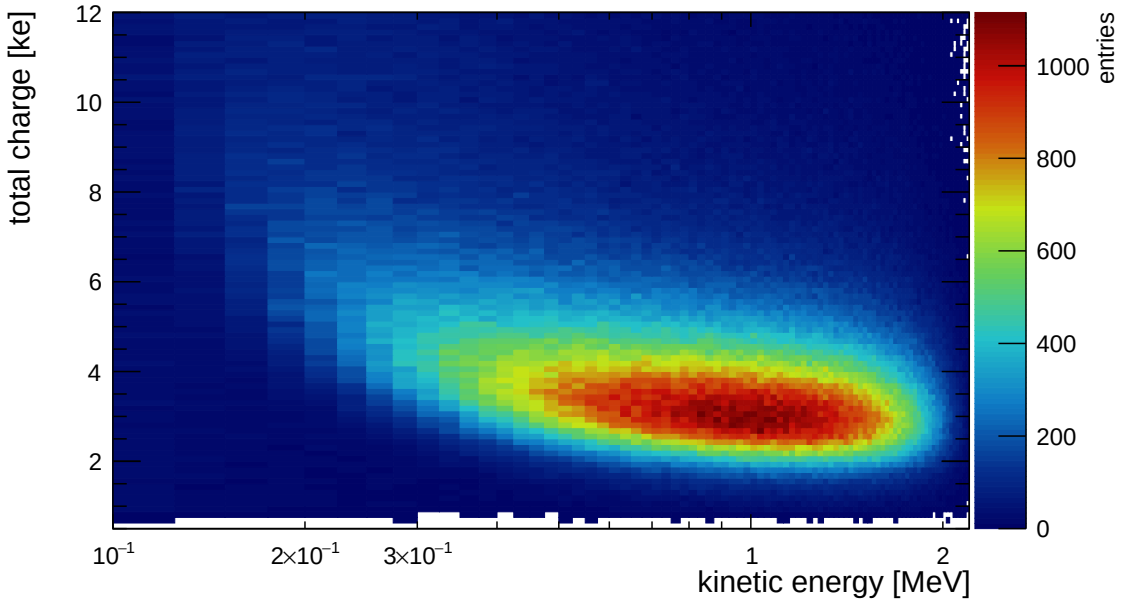

Figure 4.9: Sum of charges induced by a single electron into all pixels plotted against its kinetic energy. Data from the ^{90}Y simulation. Plotted with linear energy binning on logarithmic axis. The pixel charge range is limited for better visibility.

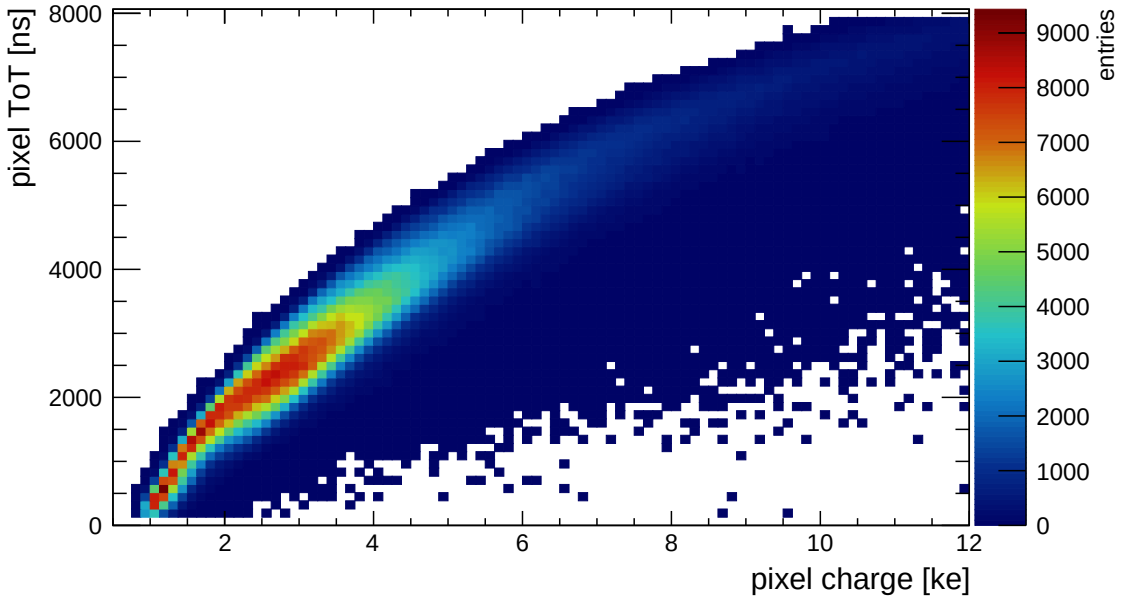

Figure 4.10: ToT from pixel against the induced charge into the corresponding pixel. Data from the ^{90}Y simulation. The ToT is cut for better visibility, excluding values smaller than 128 ns and larger than 8000 ns. The pixel charge range is limited for the same reason.

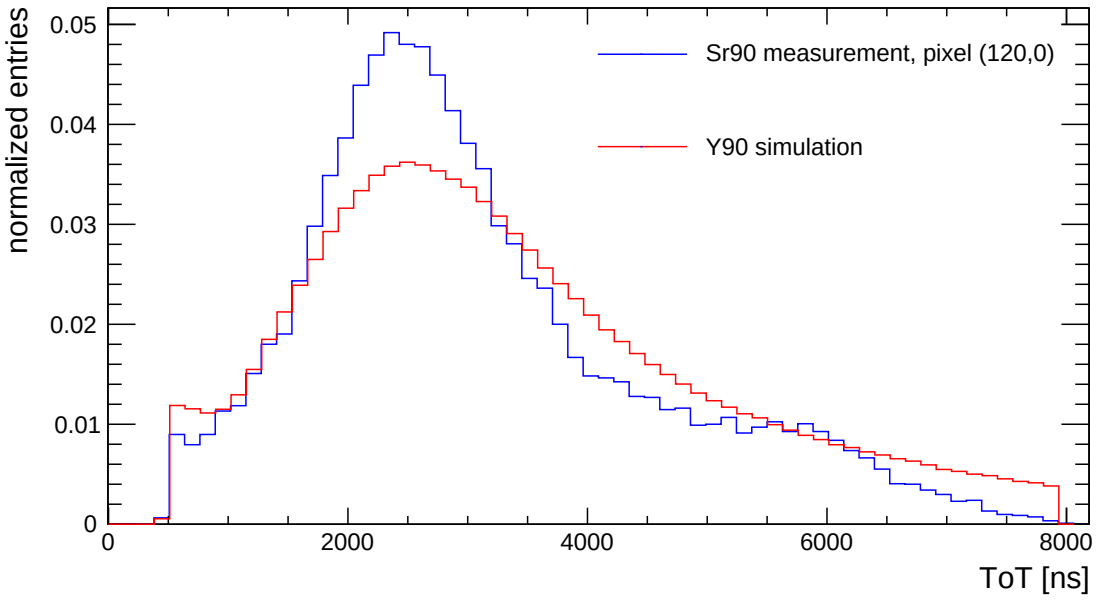

Figure 4.11: Comparison between the ToT spectrum simulated with ^{90}Y and the measured ToT spectrum of a single pixel with ^{90}Sr. The spectrum for the simulation has the same ToT cut as the measurement, excluding values smaller than 500 ns and larger than 8000 ns.

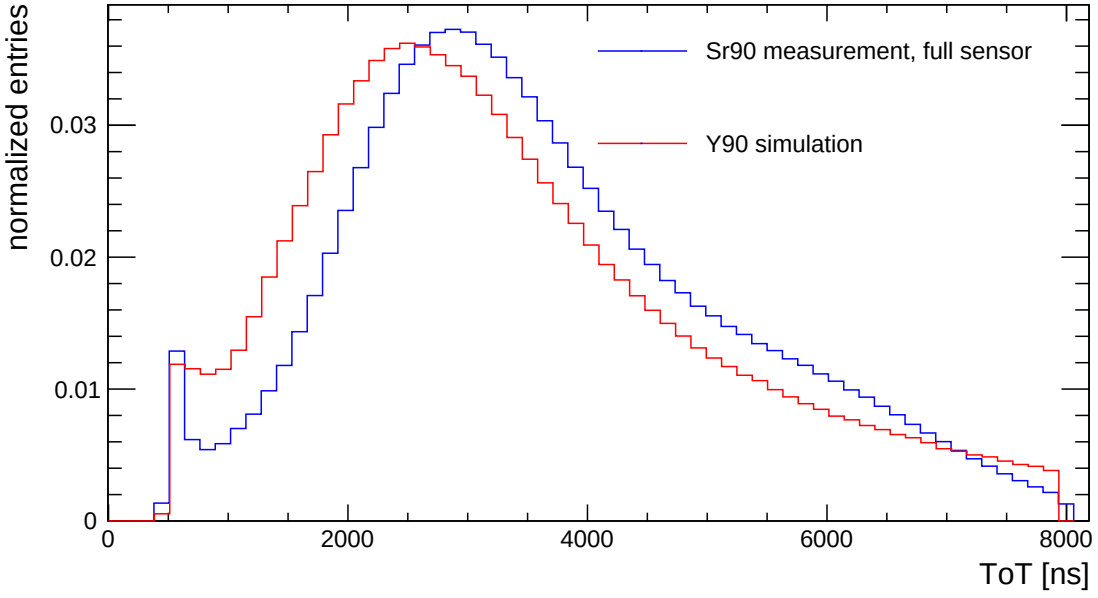

Figure 4.12: Comparison between the ToT spectrum simulated with ^{90}Y and the measured ToT spectrum of the entire sensor with ^{90}Sr. The spectrum for the simulation has the same ToT cut as the measurement, excluding values smaller than 500 ns and larger than 8000 ns.

4.4.3 Cluster Size

Figure 4.13 compares the simulated and measured cluster size distribution with the ToT cut. For cluster with a size larger than 2, the slope of the distribution between the simulation and measurement align, although the simulation has less of these cluster than measured. For cluster size 2, the measurement has more entries, and for cluster size 1 the simulation has more entries. Overall the distribution indicates that the used charge mobility model and electric field provide a good description of the charge propagation in the MuPix10. Differences could arise, aside from the mobility model and electric field, from the charge collection cut in the simulation, noise hits and pixel-to-pixel variations.

4.4.4 ToT-Energy Relation

Figure 4.10 shows the relation between the ToT of a pixel and the charge it collected. The spread in the ToT-charge relation comes from the 5 mV noise applied to the amplified pulse and the difference between the total pixel charge and the effective pixel charge after the 1 ns charge collection cut.
In Figure 4.14 the relation between ToT and kinetic energy of the electrons is shown. As electrons with low energy deposit more charge as seen before, the ToT for lower energy electrons increases. Figure 4.15 is the same plot with log scale and Figure 4.15 gives the relation for the ToT summed in all pixels. The impact of charge sharing can be seen again when comparing the distribution for low energies and low ToT of the two plots.
The plots give hints for the energy resolution of the MuPix10, however will not be discussed in-depth here as it goes beyond the scope of this thesis. For an electron with a kinetic energy of 1 MeV the ToT can vary between 2000 ns and 4000 ns. For a ToT of 3000 ns the kinetic energy of an electron can range from 300 keV and 1.5 MeV, although that value is probably capped by the maximum energy of the setup. As the energy resolution improves with a lower noise level, it is likely better than described since the estimated noise level includes noise from outside the chip.

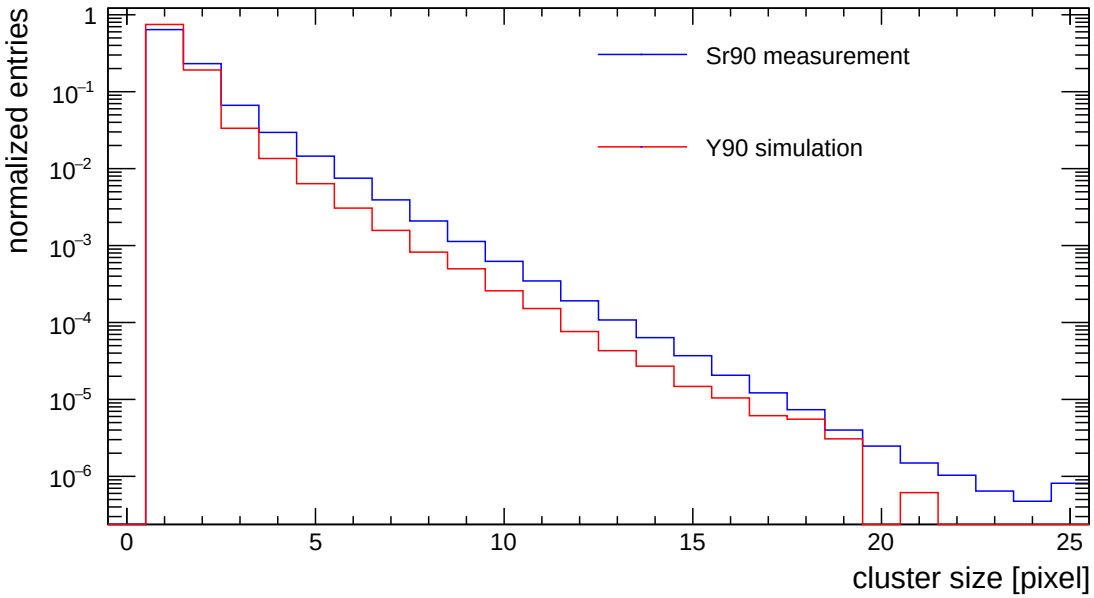

Figure 4.13: Comparison between the cluster size distribution simulated with ^{90}Y and the distribution measured with ^{90}Sr for the entire sensor. A ToT cut is applied to the measurement, excluding hits with a ToT smaller than 500 ns and larger than 8000 ns.

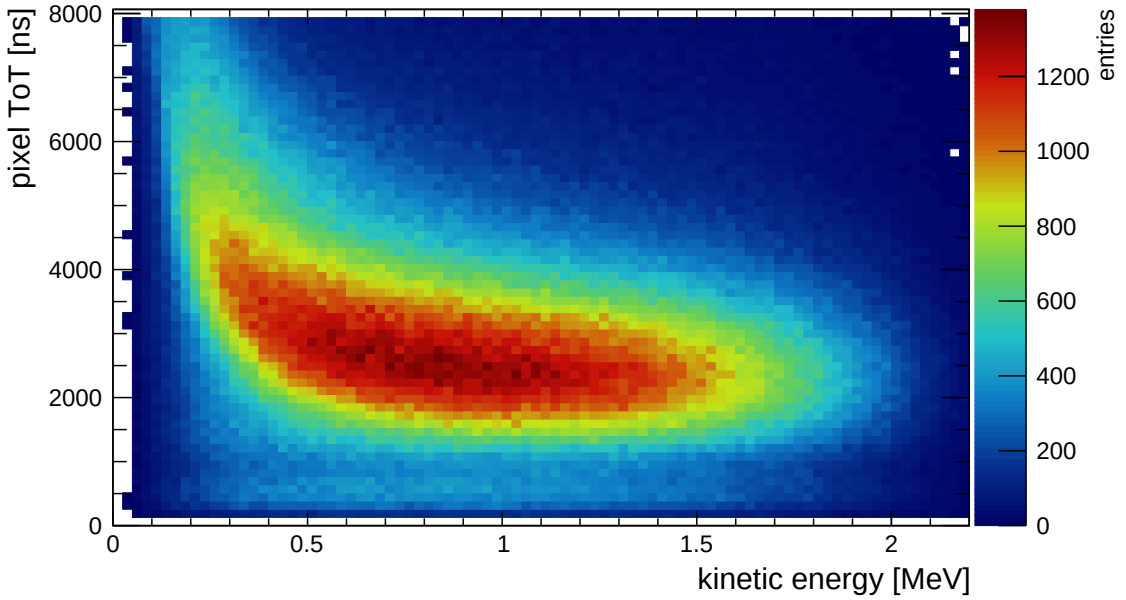

Figure 4.14: ToT from pixel plotted against the kinetic energy of the corresponding electron. Data from the ^{90}Y simulation. The ToT is cut for better visibility, excluding ToTs smaller than 128 ns and larger than 8000 ns.

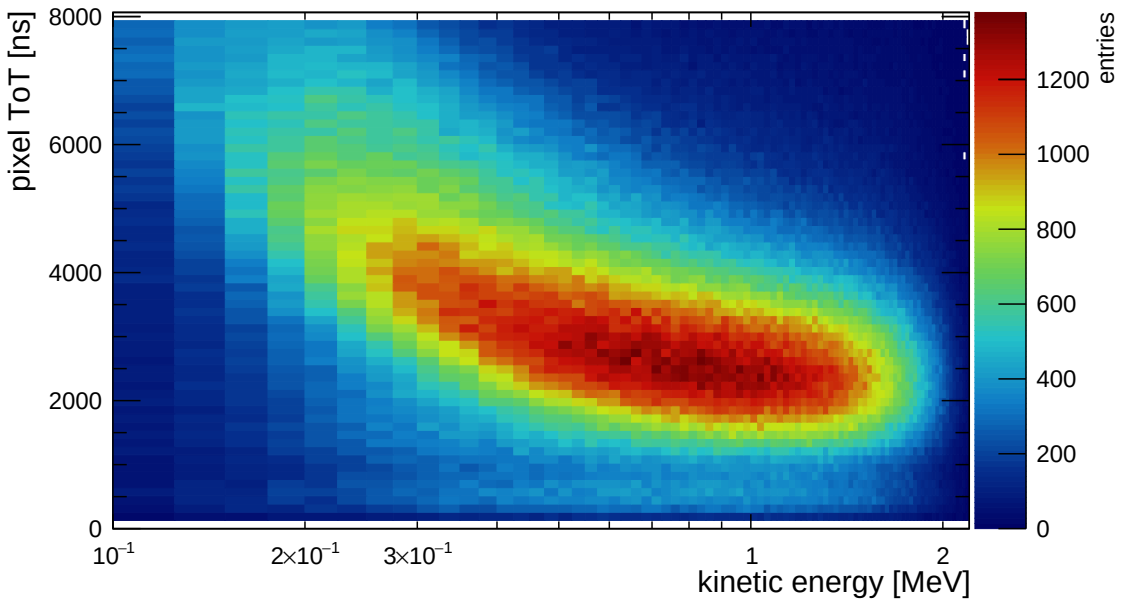

Figure 4.15: ToT from pixel plotted against the kinetic energy of the corresponding electron. Data from the ^{90}Y simulation. Plotted with linear energy binning on logarithmic axis. The ToT is cut for better visibility, excluding ToTs smaller than 128 ns and larger than 8000 ns.

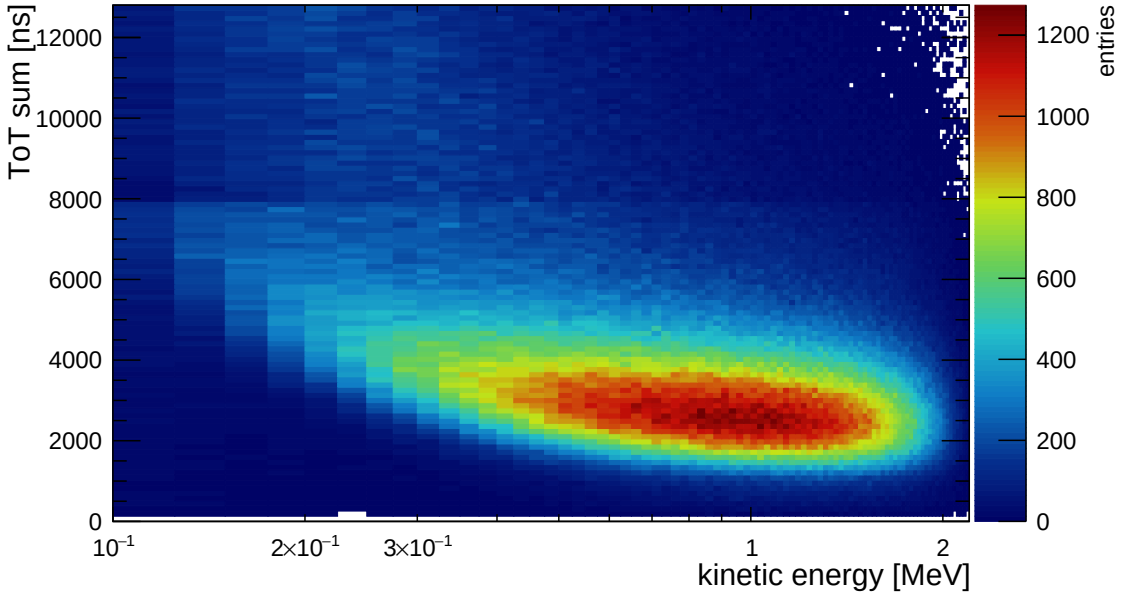

Figure 4.16: ToT sum plotted against the kinetic energy of the corresponding electron. Data from the ^{90}Y simulation. Plotted with linear energy binning on logarithmic axis. The ToT is cut for better visibility, excluding ToTs smaller than 128 ns and larger than 8000 ns.

Chapter 5

Discussion

5.1 Summary

In this thesis the pulse shape of the MuPix10 has been characterized and modeled. The model was implemented in a simulation, which was compared to measurements with ^{90}Sr. The pulses have been measured for a single pixel via an injection capacitance. An empirical model for the pulse shape was derived based on the measured waveforms. The expected difference in ToT between the modeled and measured pulses for a given threshold level was found to be smaller than two TS2 bins (256 ns).
The injection voltage dependency of the fitted amplification parameter of the pulses was investigated. The dependency was found to be linear for large injection voltages with an exponential fall for small injection voltages.
The injection capacity of the pixel was calibrated by taking pulse measurements of ^{55}Fe and its expected charge deposit in the pixel determined by a Monte Carlo simulation. The value of the injection capacity was determined to be $C_{\text{inj}} = (0.924 \pm 0.031)\,\text{fF}$, which is in agreement with the specification. The injection voltage dependency of the amplification parameter was converted to a charge dependency using the value for the injection capacity.
Measurements of ^{90}Sr with the DAQ have been done. A difference between the ToT spectrum of a single pixel and the entire sensor was found, which confirms previous studies.
The pulse shape model has been implemented in Allpix^2. Finally the ToT spectrum and cluster size of ^{90}Y have been simulated for comparison with the measurements for ^{90}Sr. The simulation was able to reproduce the ToT peak of the single pixel measurements. The simulated cluster size also roughly aligned with the measurement.
In conclusion the thesis showed that a simulation can model the charge collection and ToT behavior of the MuPix10.

5.2 Outlook

With this proof-of-concept simulation, it is worth looking into use cases of the simulation. Possible future improvements will also be discussed.

Applications The simulation can be used for characterization studies that are infeasible or complicated in the lab. For example, the ToT spectrum could be scanned for wide range of electron energies to create a ToT-to-energy parameterization. Looking into the timewalk depending on the signal size allows to study the performance of TWC methods via software and the 2-Threshold Mode. However this might require a more precise description of the rising edge and noise level. Besides comparisons using the CSA pulse, the charge collection and efficiency could be studied. An example is the impact of temperature on the charge collection. This might provide useful insight for the Mu3e detector as the temperature of the different pixel sensors can differ by several 10 K. Another example is analyzing the in-pixel efficiency. These studies could also be used for the development of future revisions of the MuPix pixel sensors.

Improvements The pulse shape used in this thesis was derived empirically and deviations from the pulse measurements are visible. Thus limitations on the accuracy are expected. A more physical approach like a transient simulation for the signal response could be derived and implemented. For the Timepix3 this is already worked on for a future `TPXDigitizer` module [44], which could be extended or adapted to work the MuPix10.
Most notably a transient simulation of the circuit would store the state of the amplifier for any given time, for example the charge a capacitance holds. However the simulation should probably make simplifications to not increase the simulation time too much. A major shortcoming with the current approach is that it excludes charges from diffusion and does not factor in the timing of the incoming charges. A transient simulation would solve this. It would allow to easily incorporate variations of components during the manufacturing process. Variations could be generated once on a pixel-by-pixel basis and kept for duration of the simulation to study calibration methods.
Besides the pulse shape, several simplifications have been made in this thesis. Crosstalk between signal lines are not simulated, but as seen in section 3.5 its impact is not negligible. It could be implemented since all hits of an event are processed at the end of the simulation chain. Possible effects of the comparator circuit are also not simulated. The injection calibration could be improved using an X-ray tube or a different more sophisticated method.

Integration Since there already exists a Geant4 simulation for the Mu3e detector [7], further steps can be taken to combine this simulation with the Mu3e simulation. Allpix^2 has a `DepositionReader` module, which allows to read ROOT files with information about the charge deposition. These ROOT files can be created easily with Geant4's built-in `G4RootAnalysisManager` using a `Ntuples` and the `G4VSensitiveDetector` class. Since Allpix^2 is a standalone simulation, the already existing digital pixel readout simulation might require changes. Using the relevant Allpix^2 modules in the Geant4 simulation is at the time of writing not trivially possible. However it might be worth to make adjustments in Allpix^2 to allow using the modules within a Geant4 simulation. This would allow to drop-in replace the existing response with a more precise Allpix^2 simulation. In addition to the ToT, the magnetic field of the detector can also be included in Allpix^2 using the `MagneticFieldReader` module to simulate the Lorentz shift.

Appendix A

Experimental Settings

Variable	Value
Number	V1 21
Thickness	625 µm
Resistivity	200 Ω cm

Table A.1: Chip model.

Output	Voltage	Current
High-Voltage	−100 V	0.4 µA
VDDA	2.315 V	700 mA

Table A.2: External power values.

Output	Voltage
gnda1	0.294 V
vdda1	2.091 V
vssa1	1.291 V
gnd1	0.058 V
vdd1	2.276 V
BLpix	1.099 V
BLdig	0.797 V
THlo	0.831 V
nFOLL	0.638 V
nFB	0.022 V
nAMP	1.070 V
pLoad	1.435 V
Nout	0.925 V
BLrPix	0.647 V

Table A.3: Chip voltages measured on the insert.

Variable	Setting
Duration	40 µs
Frequency	50 Hz
Pixel column	120
Pixel row	0

Table A.4: Used injection settings.

DAC	Setting [hex]
BLResPix	5
VNPix	14
VNFBPix	4
VNFollPix	c
VNDel	a
VPComp1	0
VNPix2	0
BLResDig	5
VNBiasPix	0
VPLoadPix	a
VPVCO	22
VPVNCO	23
VNLVDS	14
VPComp2	5
VPFoll	14
VPTimerDel	1
VNTimerDel	14
ckdivend	0
ckdivend2	1f
ref_Vss	c3
Baseline	47
ThLow	4c
ThHigh	0
ThPix	0
BLPix	72

Table A.5: Used DAC configuration.

Appendix B

Notes on the Pulse Shape Fitting

The pulse shape function written in C++ for fitting with ROOT:

```
#include <cmath>


// Function for fitting with ROOT
double MuPixPulseFitFunction(double* x, double* par)
{
    // Get function variables
    const double t = x[0];

    // Get function parameters
    const double timestep = par[0];  // Integration step size, e.g. 0.001 us
    const double t_0      = par[1];  // Time offset, e.g. 0 us
    const double U_0      = par[2];  // Voltage offset, e.g. 0 mV
    const double A        = par[3];  // Amplification parameter, e.g. 250 mV
    const double t_R      = par[4];  // Amplification rise time parameter, e.g. 0.1 us
    const double t_F      = par[5];  // Amplification fall time parameter, e.g. 4.8 us
    const double t_S      = par[6];  // Amplification smoothing parameter, e.g. 0.1 us
    const double Fb       = par[7];  // Feedback fall rate, e.g. 23 mV/us
    const double Fb_D     = par[8];  // Feedback damping parameter, e.g. 2 mV
    const double U_sat    = par[9];  // Saturation voltage, e.g. 360 mV

    // // Lambda for double-exponential amplification with smoothing
    auto Amplification = [=](double t) -> double
    {
        const double rise = 1. - exp(-t / t_R);
        const double fall = exp(-t / t_F) - 1.;
        const double smoothing = 1. - exp(-t / t_S);
        return A * (rise + fall) * smoothing;
    };

    // Lambda for quasi-constant feedback with exponential damping for small signals
    auto Feedback = [=](double U) -> double
    {
        return Fb * (1. - exp(-U / Fb_D));
    };

    // Lambda for saturation at maximum voltage using the logistic function
    auto Saturation = [=](double U) -> double
    {
        return U_sat * (2. / (1. + exp(-2. * U / U_sat)) - 1.);
    };
```

```
    // Remove time offset to get evaluation time and number of iterations
    const double t_eval = t - t_0;
    const int iterations = static_cast<int>(std::ceil(t_eval / timestep));

    // Prepare output variable
    double U_out = 0.;

    // Prepare cache variable for amplification output
    double U_amp_t_n   = 0.;
    double U_amp_t_nm1 = 0.;

    // Loop over time
    for (auto n = 1; n < iterations; ++n)
    {
        // Calculate amplification output
        U_amp_t_n = Amplification(static_cast<double>(n) * timestep);

        // Add amplification difference to output
        U_out += (U_amp_t_n - U_amp_t_nm1);

        // Cache amplification output for next iteration
        U_amp_t_nm1 = U_amp_t_n;

        // Subtract feedback
        U_out -= Feedback(U_out) * timestep;
    }

    // Apply saturation
    U_out = Saturation(U_out);

    // Add voltage offset
    U_out += U_0;

    // Return result
    return U_out;
}
```

The function given above is quite expensive to compute and on top is quite unstable to fit. The standard fitting procedure in ROOT failed to converge most of the time. As a consequence, a combination of two algorithms was used to fit the function.
Before fitting, U_0 is fixed by taking the average of the voltage before the signal response and t_0 is estimated from the rising edge. Then the function is fitted until the maximum using the `Minuit2` library with the `Simplex` minimization algorithm. This is done to determine t_0. Compared to the default `Migrad` algorithm, `Simplex` is much less sensitive to the precision of the function. As the function is integrated in time steps and thus has artifacts, `Migrad` is often not capable to vary t_0 from the initial guess at all, resulting in a failed fit. However `Simplex` also has disadvantages, its *expected distance to the minimum* (Edm) is quote "largely fantasy" and is not reliable with respect to parameter errors [45]. For this reason, the second fit uses the `Migrad` algorithm.
Overall, this method gives good results in a reasonable amount of time (between 3 s and 30 s per waveform, depending on the length of the signal). It should be noted that this is not the most efficient way for fitting, as the consecutive function calls with the same parameter set all start iterating from the beginning.

Appendix C

Pulse Fits

Pulse	Amplification parameter	Pulse	Amplification parameter
Iron-55	(91.21 ± 1.13) mV	800 mV	(397.82 ± 0.81) mV
200 mV	(58.55 ± 0.67) mV	900 mV	(463.94 ± 0.86) mV
300 mV	(101.80 ± 0.62) mV	1000 mV	(533.26 ± 0.93) mV
400 mV	(153.29 ± 0.63) mV	1100 mV	(595.93 ± 0.99) mV
500 mV	(208.77 ± 0.66) mV	1200 mV	(662.31 ± 1.05) mV
600 mV	(268.84 ± 0.69) mV	1300 mV	(725.23 ± 1.13) mV
700 mV	(331.17 ± 0.75) mV	1400 mV	(788.94 ± 1.21) mV

Table C.1: Fit results for the amplification parameter.

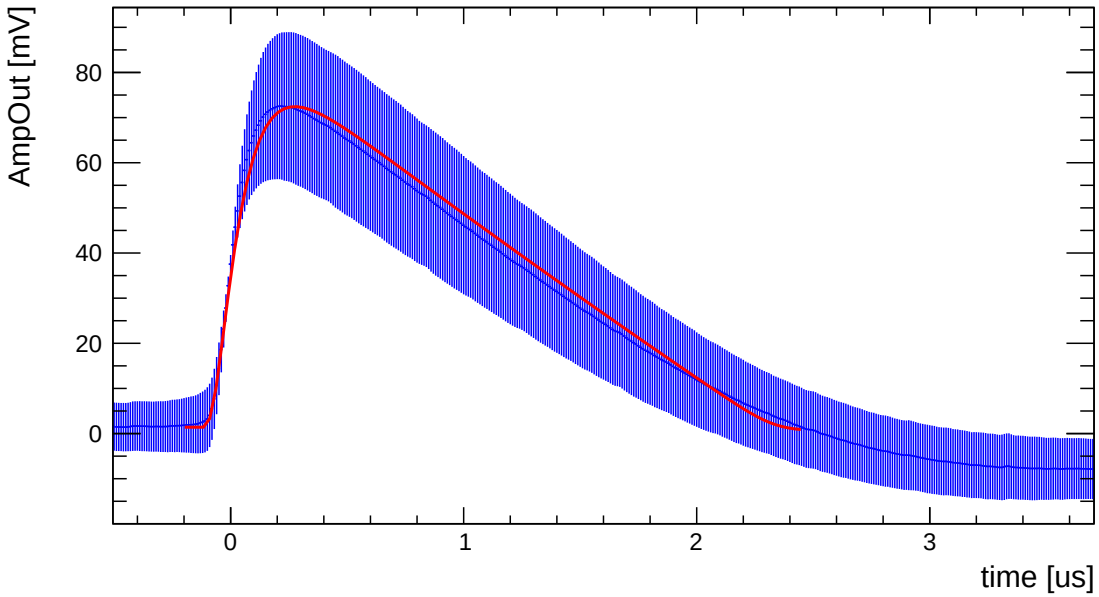

Figure C.1: Pulse fit for Fe55.

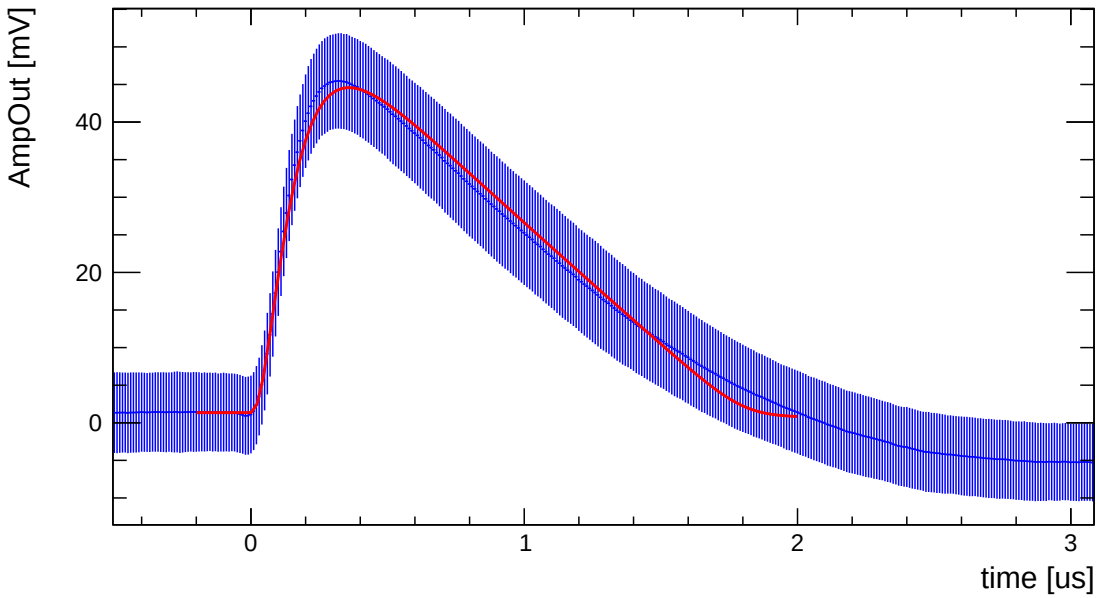

Figure C.2: Pulse fit for 200 mV injection.

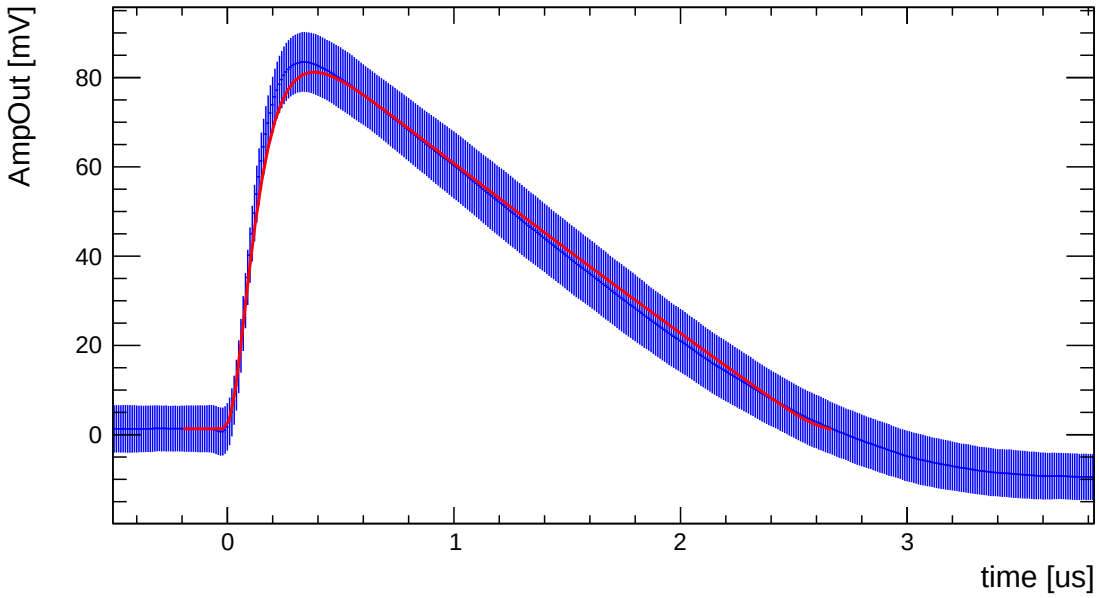

Figure C.3: Pulse fit for 300 mV injection.

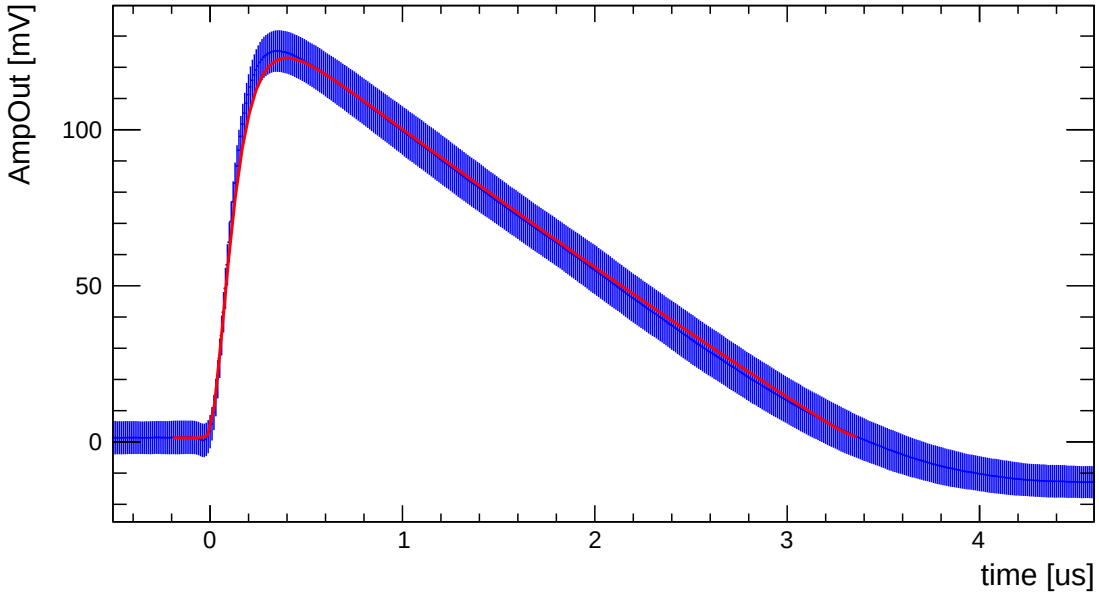

Figure C.4: Pulse fit for 400 mV injection.

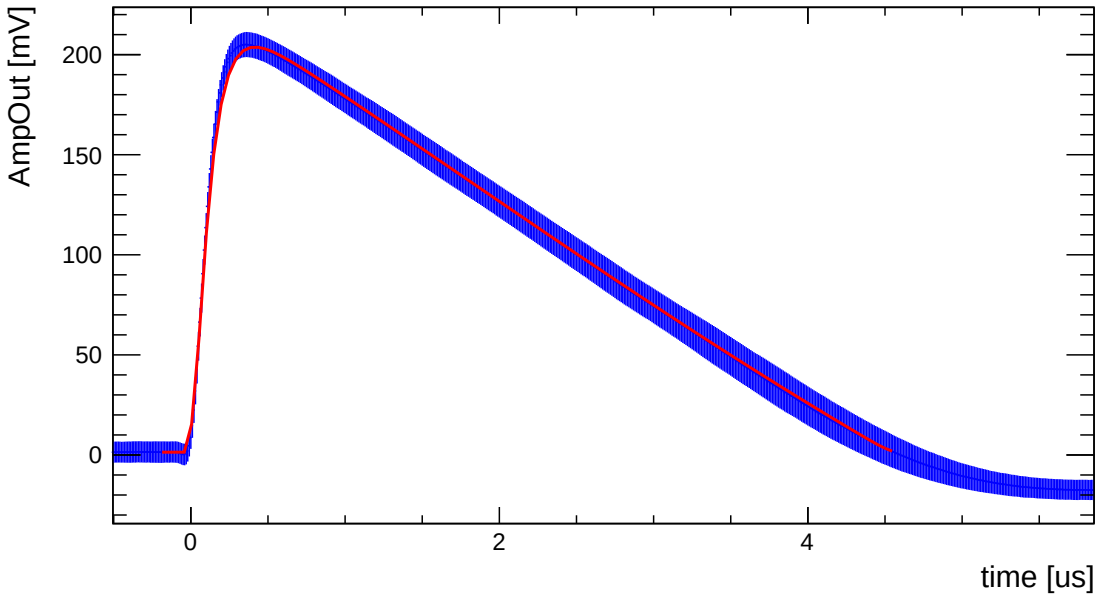

Figure C.5: Pulse fit for 600 mV injection.

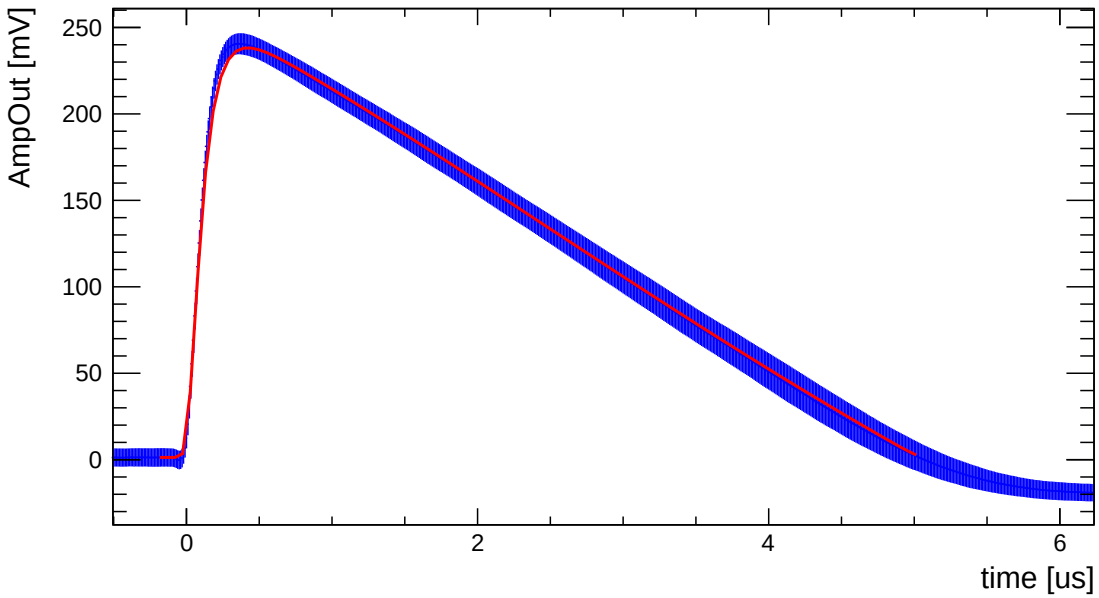

Figure C.6: Pulse fit for 700 mV injection.

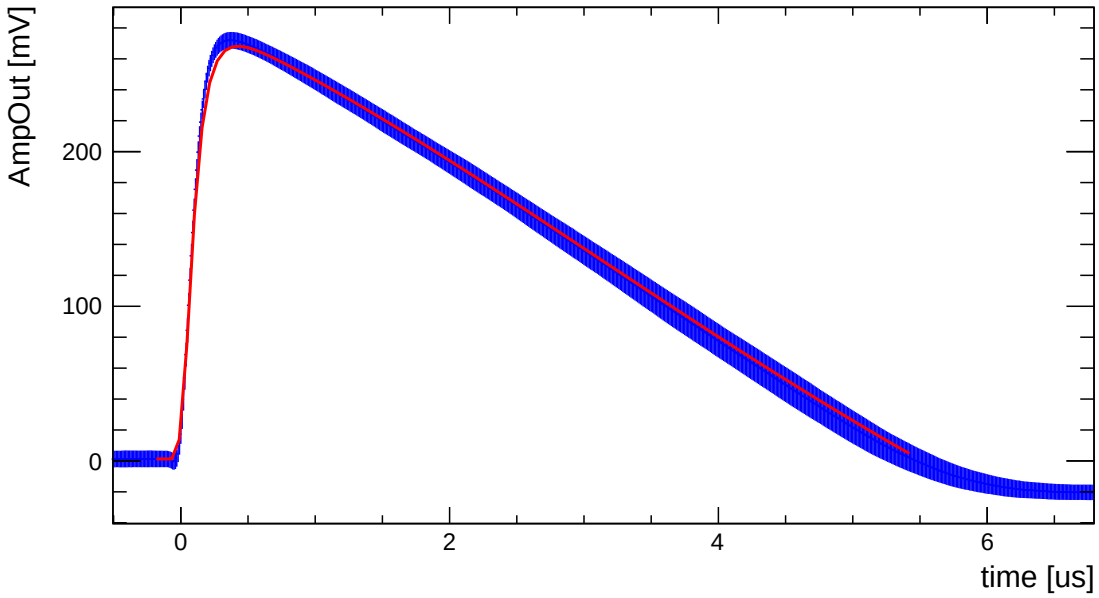

Figure C.7: Pulse fit for 800 mV injection.

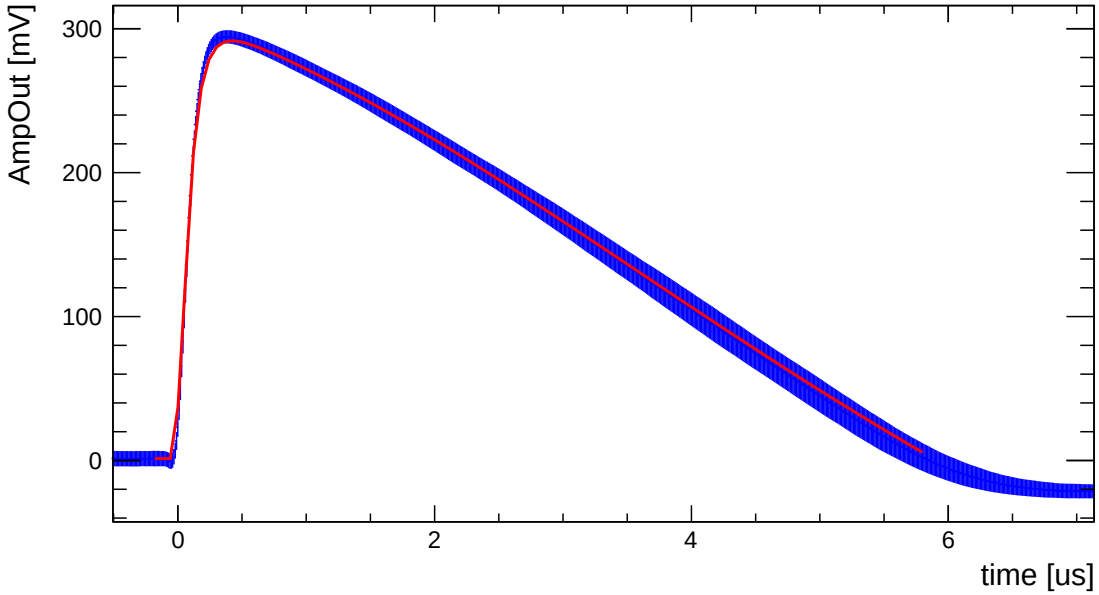

Figure C.8: Pulse fit for 900 mV injection.

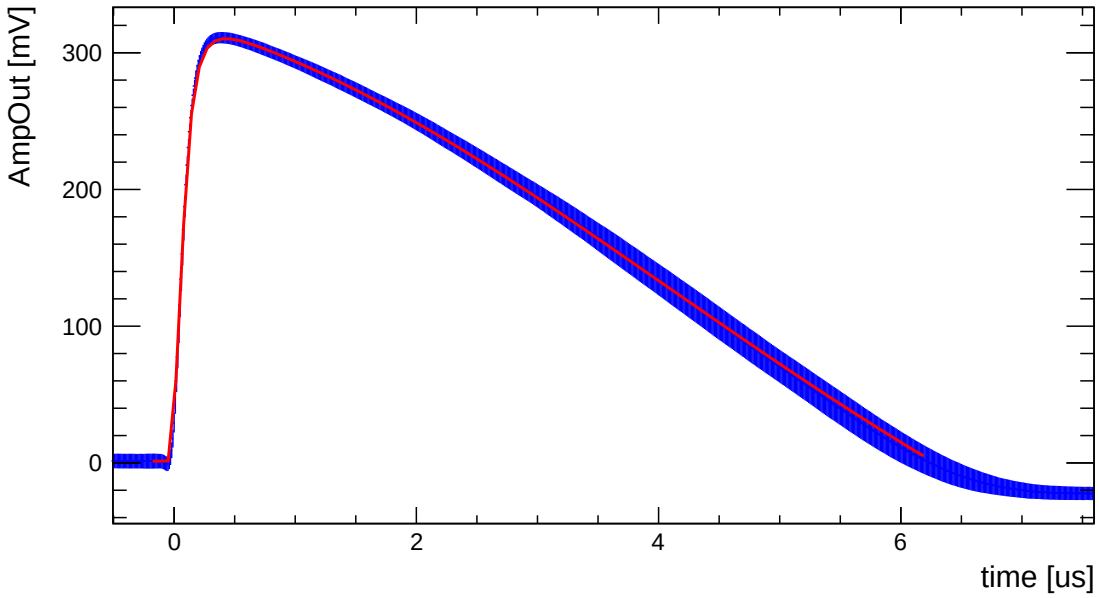

Figure C.9: Pulse fit for 1000 mV injection.

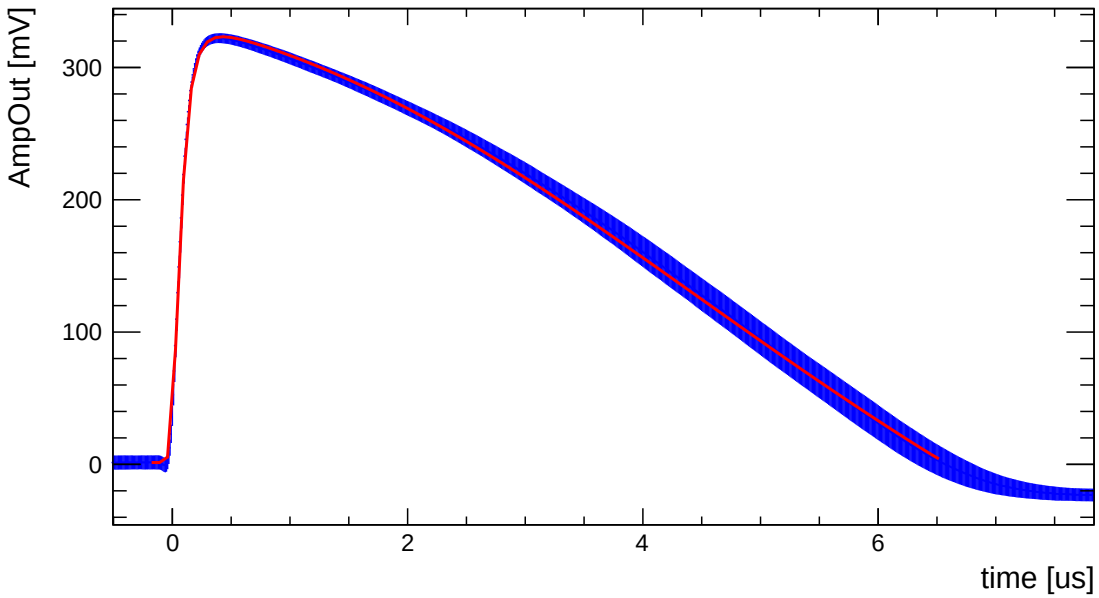

Figure C.10: Pulse fit for 1100 mV injection.

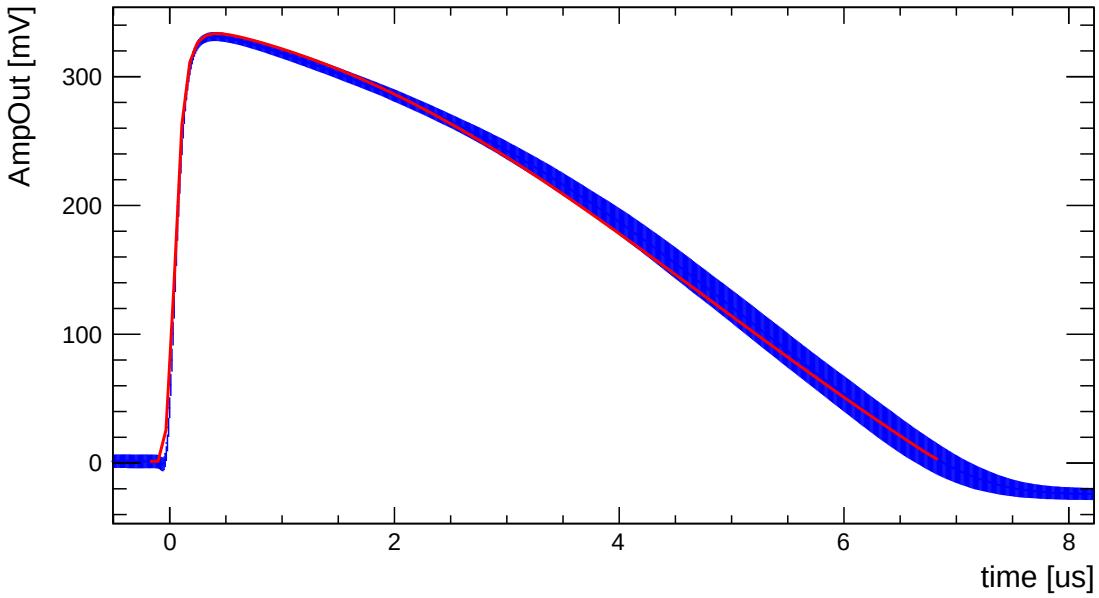

Figure C.11: Pulse fit for 1200 mV injection.

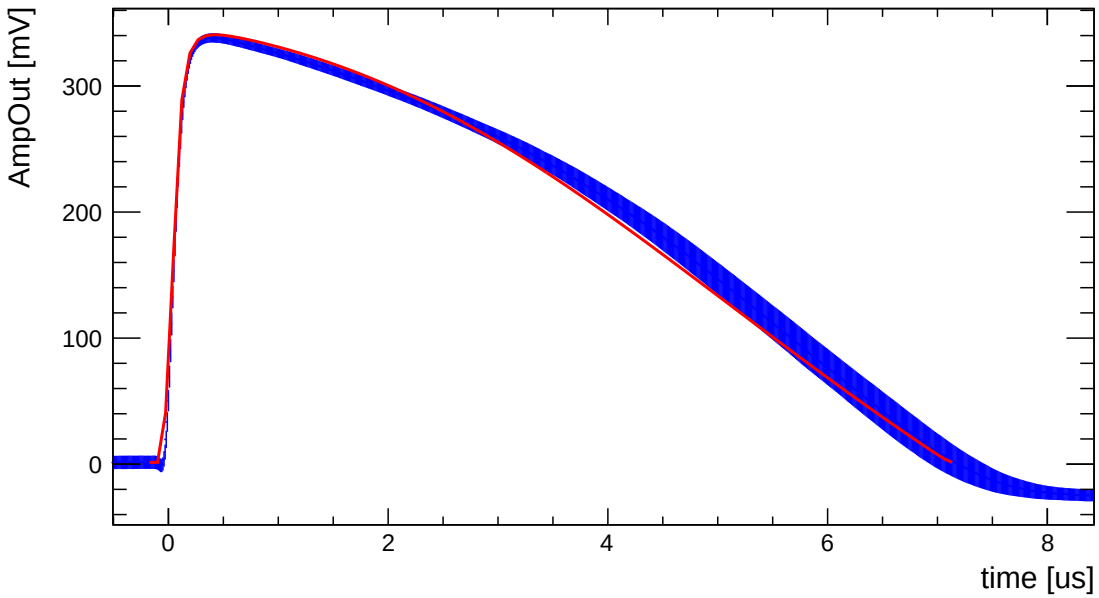

Figure C.12: Pulse fit for 1300 mV injection.

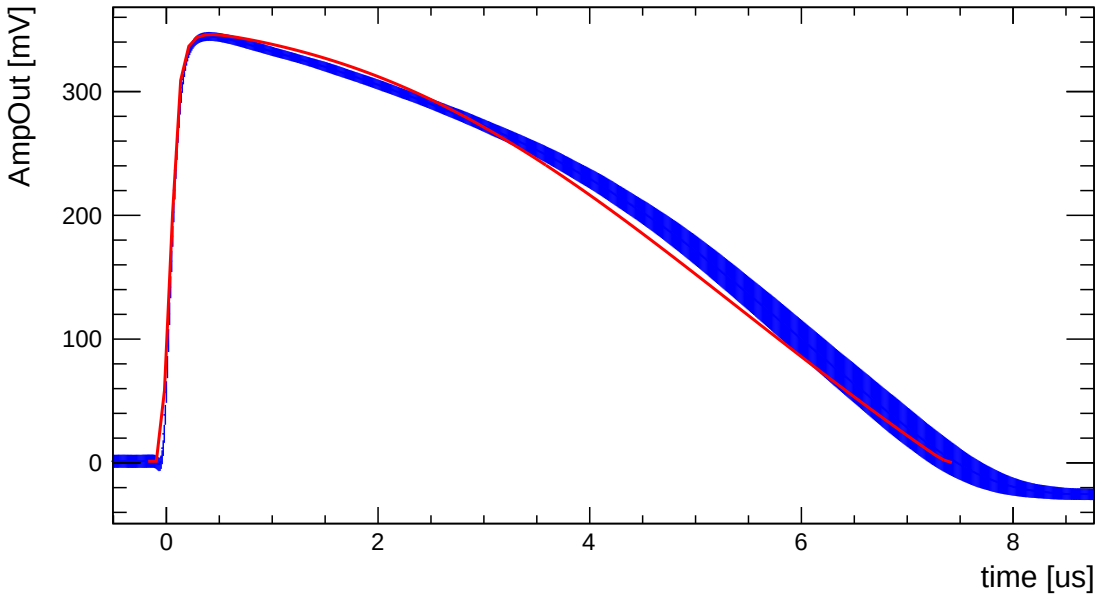

Figure C.13: Pulse fit for 1400 mV injection.

Appendix D

DESY testbeam simulation

In Figure D.1 a comparison between the ToT spectrum recorded on a testbeam at DESY with a simulation. The electrons at DESY have an energy of 4 GeV. The chip different than the one used in the thesis. It had a thickness of 100 µm. The high-voltage was 100 V and the threshold level 35 mV. The ToT cap was set to (3500 ± 120) ns in the simulation. Besides the adjusted threshold and different source, the same settings as for the ^{90}Sr simulation were used. The results shall not be discussed within this thesis.

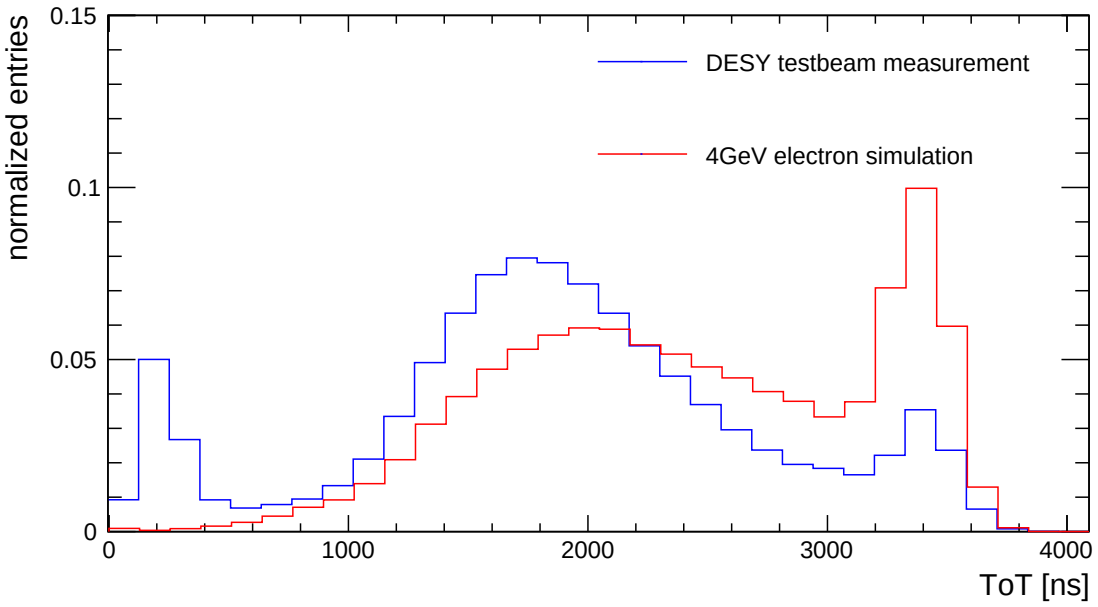

Figure D.1: Simulated ToT spectrum for 4 GeV electrons like at the DESY.

List of Figures

List of Tables

Bibliography

[1] A. Blondel et al. *Research Proposal for an Experiment to Search for the Decay $\mu \to eee$*. 2013-01. arXiv: 1301.6113.

[2] Wikimedia Commons. *Standard Model of Elementary Particles*. 2021. URL: https://commons.wikimedia.org/w/index.php?title=File:Standard_Model_of_Elementary_Particles.svg&oldid=585729208 (visited on 2021-08-29).

[3] Y. Fukuda et al. „Evidence for Oscillation of Atmospheric Neutrinos." In: *Phys. Rev. Lett.* 81.8 (1998-08), pp. 1562–1567. ISSN: 1079-7114. DOI: 10.1103/PhysRevLett.81.1562. arXiv: hep-ex/9807003.

[4] Yoshitaka Kuno and Yasuhiro Okada. „Muon decay and physics beyond the standard model." In: *Rev. Mod. Phys.* 73.1 (2001-01), pp. 151–202. ISSN: 1539-0756. DOI: 10.1103/RevModPhys.73.151. arXiv: hep-ph/9909265.

[5] G. Hernández-Tomé, G. López Castro, and P. Roig. „Flavor violating leptonic decays of τ and μ leptons in the Standard Model with massive neutrinos." In: *The European Physical Journal C* 79 (2019-01), p. 84. ISSN: 1434-6052. DOI: 10.1140/epjc/s10052-019-6563-4. arXiv: 1807.06050.

[6] Mu3e Collaboration. Internal Notes.

[7] K. Arndt et al. *Technical design of the phase I Mu3e experiment*. 2021-02. arXiv: 2009.11690.

[8] U. Bellgardt et al. „Search for the decay $\mu^+ \to e^+ e^- e^+$." In: *Nuclear Physics B* 299 (1988), pp. 1–6. ISSN: 0550-3213. DOI: 10.1016/0550-3213(88)90462-2.

[9] William J. Marciano, Toshinori Mori, and J. Michael Roney. „Charged Lepton Flavor Violation Experiments." In: *Annual Review of Nuclear and Particle Science* 58 (2008), pp. 315–341. ISSN: 1545-4134. DOI: 10.1146/annurev.nucl.58.110707.171126.

[10] H. Bethe and J. Ashkin. In: *Experimental nuclear physics*. Ed. by Emilio Segrè. 1953.

[11] M. Tanabashi et al. „Review of Particle Physics." In: *Phys. Rev. D* 98.3 (2018), p. 030001. ISSN: 1550-7998. DOI: 10.1103/PhysRevD.98.030001.

[12] Stephen M. Seltzer and Martin J. Berger. „Improved procedure for calculating the collision stopping power of elements and compounds for electrons and positrons." In: *The International Journal of Applied Radiation and Isotopes* 35.7 (1984), pp. 665–676. ISSN: 0020-708X. DOI: 10.1016/0020-708X(84)90113-3.

[13] Heiko Augustin. „Characterization of a novel HV-MAPS Sensor with two Amplification Stages and first examination of thinned MuPix Sensors." Master thesis. Heidelberg University, 2014. URL: https://www.physi.uni-heidelberg.de/Publications/Thesis.Augustin.pdf.

[14] Virgil L. Highland. „Some practical remarks on multiple scattering." In: *Nuclear Instruments and Methods* 129.2 (1975), pp. 497–499. ISSN: 0029-554X. DOI: 10.1016/0029-554X(75)90743-0.

[15] D. Durini and D. Arutinov. „Operational principles of silicon image sensors.“ In: *High Performance Silicon Imaging (Second Edition)*. Ed. by Daniel Durini. Second Edition. Woodhead Publishing Series in Electronic and Optical Materials. Woodhead Publishing, 2020, pp. 25–73. ISBN: 978-0-08-102434-8. DOI: 10.1016/B978-0-08-102434-8.00002-7.

[16] John J. Smithrick and Ira T. Myers. „Average Triton Energy Deposited in Silicon per Electron-Hole Pair Produced.“ In: *Phys. Rev. B* 1.7 (1970-04), pp. 2945–2948. DOI: 10.1103/PhysRevB.1.2945.

[17] Wikimedia Commons. *Pn junction equilibrium graphs*. 2007-08. URL: https://commons.wikimedia.org/w/index.php?title=File:Pn-junction-equilibrium-graphs.png&oldid=451423606 (visited on 2021-07-13).

[18] Ivan Perić. „A novel monolithic pixelated particle detector implemented in high-voltage CMOS technology.“ In: *Nuclear Instruments and Methods in Physics Research Section A: Accelerators, Spectrometers, Detectors and Associated Equipment* 582.3 (2007), pp. 976–885. ISSN: 0168-9002. DOI: 10.1016/j.nima.2007.07.115.

[19] Jens Kröger. „Characterisation of a High-Voltage Monolithic Active Pixel Sensor Prototype for Future Collider Detectors.“ Dissertation. Heidelberg University, 2021.

[20] Wikipedia contributors. *Monte Carlo method*. 2021. URL: https://en.wikipedia.org/w/index.php?title=Monte_Carlo_method&oldid=1041801849 (visited on 2021-09-07).

[21] John Allison et al. *Geant4*. URL: https://geant4.web.cern.ch/.

[22] S. Agostinelli et al. „Geant4 – a simulation toolkit.“ In: *Nuclear Instruments and Methods in Physics Research Section A: Accelerators, Spectrometers, Detectors and Associated Equipment* 506.3 (2003), pp. 250–303. ISSN: 0168-9002. DOI: 10.1016/S0168-9002(03)01368-8.

[23] J. Allison et al. „Recent developments in Geant4.“ In: *Nuclear Instruments and Methods in Physics Research Section A: Accelerators, Spectrometers, Detectors and Associated Equipment* 835 (2016), pp. 186–225. ISSN: 0168-9002. DOI: 10.1016/j.nima.2016.06.125.

[24] Rene Brun and Fons Rademakers. „ROOT – An object oriented data analysis framework.“ In: *Nuclear Instruments and Methods in Physics Research Section A: Accelerators, Spectrometers, Detectors and Associated Equipment* 389.1 (1997), pp. 81–86. ISSN: 0168-9002. DOI: 10.1016/S0168-9002(97)00048-X. eprint: https://cds.cern.ch/record/491486/files/p11.pdf.

[25] Axel Naumann et al. *ROOT – Data Analysis Framework*. DOI: 10.5281/zenodo.848818. URL: https://root.cern/.

[26] S. Spannagel et al. „Allpix2: A modular simulation framework for silicon detectors.“ In: *Nuclear Instruments and Methods in Physics Research Section A: Accelerators, Spectrometers, Detectors and Associated Equipment* 901 (2018), pp. 164–172. ISSN: 0168-9002. DOI: 10.1016/j.nima.2018.06.020. arXiv: 1806.05813.

[27] Simon Spannagel, Koen Wolters, and Paul Schütze. *Allpix Squared – Generic Pixel Detector Simulation Framework*. DOI: 10.5281/zenodo.3550935. URL: https://cern.ch/allpix-squared/.

[28] Marius Wilm Menzel. „Calibration of the MuPix10 Pixel Sensor for the Mu3e Experiment.“ Bachelor thesis. Heidelberg University, 2020.

[29] Heiko Augustin et al. „MuPix10: First Results from the Final Design.“ In: *JPS Conf. Proc.* 34 (2021), p. 010012. ISSN: 2435-3892. DOI: 10.7566/JPSCP.34.010012. arXiv: 2012.05868.

[30] Jan Patrick Hammerich. „Analog Characterization and Time Resolution of a large scale HV-MAPS Prototype.“ Master thesis. Heidelberg University, 2018. URL: https://www.physi.uni-heidelberg.de/Publications/MasterHammerich.pdf.

[31] Lennart Huth. „A High Rate Testbeam Data Acquisition System and Characterization of High Voltage Monolithic Active Pixel Sensors.“ Dissertation. Heidelberg University, 2018. DOI: 10.11588/heidok.00025785.

[32] Tektronix. *DPO7000 Series Datasheet*. 2018. URL: https://download.tek.com/datasheet/DPO7000C-Oscilloscope-Datasheet-48W2654321.pdf (visited on 2021-06-07).

[33] Wikimedia Commons. *Iron-55*. 2021. URL: https://en.wikipedia.org/w/index.php?title=Iron-55&oldid=1031111223 (visited on 2021-08-29).

[34] Wikimedia Commons. *Strontium-90*. 2021. URL: https://en.wikipedia.org/w/index.php?title=Strontium-90&oldid=1039989937 (visited on 2021-08-29).

[35] Helmuth Spieler. *Introduction to Radiation Detectors and Electronics – V.3. Semiconductor Detectors – Resolution and Signal-to-Noise Ratio*. 1999. URL: https://www-physics.lbl.gov/~spieler/physics_198_notes_1999/PDF/V-3-Resolution-2.pdf (visited on 2021-09-04).

[36] Patrick McCormack et al. „New Method for Silicon Sensor Charge Calibration Using Compton Scattering.“ In: (2020). arXiv: 2008.11860.

[37] Florian Frauen. „Characterisation of the time resolution of the MuPix10 pixel sensor.“ Bachelor thesis. Heidelberg University, 2021.

[38] Annie Meneses González. Private Communication.

[39] C. Scharf and R. Klanner. „Measurement of the drift velocities of electrons and holes in high-ohmic <100> silicon.“ In: *Nuclear Instruments and Methods in Physics Research Section A: Accelerators, Spectrometers, Detectors and Associated Equipment* 799 (2015), pp. 81–89. ISSN: 0168-9002. DOI: 10.1016/j.nima.2015.07.057. arXiv: 1806.05813.

[40] W. Shockley and W. T. Read. „Statistics of the Recombinations of Holes and Electrons.“ In: *Phys. Rev.* 87.5 (1952-09), pp. 835–842. DOI: 10.1103/PhysRev.87.835.

[41] R. N. Hall. „Electron-Hole Recombination in Germanium.“ In: *Phys. Rev.* 87.2 (1952-07), pp. 387–387. DOI: 10.1103/PhysRev.87.387.

[42] J. Dziewior and W. Schmid. „Auger coefficients for highly doped and highly excited silicon.“ In: *Applied Physics Letters* 31.5 (1977), pp. 346–348. DOI: 10.1063/1.89694.

[43] Rafal Kleczek, Pawel Grybos, and Robert Szczygiel. „Charge sensitive amplifier for nanoseconds pulse processing time in CMOS 40 nm technology.“ In: *2015 22nd International Conference Mixed Design of Integrated Circuits Systems (MIXDES)*. 2015, pp. 292–296. DOI: 10.1109/MIXDES.2015.7208529.

[44] Lukas Tlustos and Pinelopi Christodoulou. *Digitizer plug-in for Krummenacher CSA*. 2nd Allpix Squared User Workshop. 2021-08-19. URL: https://indico.cern.ch/event/1043567/contributions/4467494 (visited on 2021-08-20).

[45] Fred James and Matthias Winkler. *ROOT Online Guide for Minuit 2*. URL: https://root.cern.ch/root/htmldoc/guides/minuit2/Minuit2.html#which-minimizer-to-use (visited on 2021-08-31).

Acknowledgments

First, I want to thank Prof. André Schöning for giving me the great opportunity to write my thesis in this amazing group.

Thanks to Peter Fischer, the second examiner of my thesis.

To Dohun Kim, David Immig and Heiko Augustin: thank you so much for helping me in nearly all aspects of this thesis, from debugging measurements to explaining the behavior of the MuPix10. Without you, this thesis would have been much shorter and more diffuse.

I acknowledge Dohun Kim for running the analysis of the digital data, Heiko Augustin for coming up with the basis of the pulse shape function used in this thesis, Annie Meneses González for providing the TCAD files, Luigi Vigani for explaining the injection calibration concept and Jakob Stricker for giving me the analyzed data from the DESY testbeam.

I also acknowledge the work of all contributor to the Allpix^2 project, especially Simon Spannagel and Paul Schütze for their great communication.

My thanks also go to all other members of the Mu3e and HE group at the PI that helped me with all sorts of things and made me having a great time, as well as all current and past members of the Mu3e experiment allowing me to work on such an amazing experiment.

I thank Luigi, Sebastian, Dohun, David, Jan, Jona and Mauritz for reviewing my thesis.

Finally, I would like to thank my parents for their love and support of my studies.

Erklärung

Ich versichere, dass ich diese Arbeit selbstständig verfasst habe und keine anderen als die angegebenen Quellen und Hilfsmittel benutzt habe.

Heidelberg, den 18. September 2021,